

Non-Intrusive Diagnostics of Outdoor Ceramic Insulators Using Ultrasonic Signatures and Deep Learning Models

by

Abdulla Eyad Lutfi

A thesis

presented to the University of Waterloo

in fulfillment of the

thesis requirement for the degree of

Doctor of Philosophy

in

Electrical and Computer Engineering

Waterloo, Ontario, Canada, 2025

© Abdulla Eyad Lutfi 2025

Examining Committee Membership

The following served on the Examining Committee for this thesis. The decision of the Examining Committee is by majority vote.

Supervisor:	Ayman El-Hag Associate Professor, Teaching Stream Department of Electrical and Computer Engineering University of Waterloo
Co-Supervisor:	Khaled Shaban Professor, Department of Computer Science and Engineering Qatar University
Internal Member	Ramadan El-Shatshat Associate Professor, Teaching Stream, Department of Electrical and Computer Engineering University of Waterloo
Internal Member	Refat Ghunem Adjunct Assistant Professor. Department of Electrical and Computer Engineering University of Waterloo
Internal-External Member	William Melek Professor, University Research Chair, and RoboHub Director Department of Mechanical and Mechatronics Engineering University of Waterloo
External Examiner	William A. Chisholm Adjunct Lecturer. Department of Electrical and Computer Engineering University of Toronto

Author's Declaration

I hereby declare that I am the sole author of this thesis. This is a true copy of the thesis, including any required final revisions, as accepted by my examiners.

I understand that my thesis may be made electronically available to the public.

Abstract

Ceramic insulators have been widely used in overhead power lines for over a century. However, in recent years, transmission and distribution networks have been gradually shifting toward polymeric insulators. Despite this transition, many ceramic insulators remain in service, and a significant portion are now approaching or exceeding their intended lifespans. This aging infrastructure poses an increasing risk of sudden failure, thereby compromising network reliability. Insulator failures account for nearly half of maintenance costs in transmission lines [1], prompting a growing demand among utilities for fast, reliable, and cost-effective condition monitoring systems.

Defective ceramic insulators that experience internal punctures, broken discs, or cracks will ultimately initiate partial discharge (PD) activities. Additionally, ceramic insulators exposed to high contamination levels are prone to dry band arcing (DBA), which increases the risk of flashover. Both PD and DBA emit electromagnetic, ultraviolet, infrared and/or ultrasonic radiation, serving as critical indicators that can trigger corrective maintenance actions. Employing sensors to detect these early-stage discharge activities is essential for preventing insulator failure and reducing the risk of power outages. Furthermore, insulator strings often exhibit multiple concurrent defects, resulting in various discharge activities—such as corona, PD, or DBA—each characterized by distinct properties. The overlapping nature of these discharge activities poses significant challenges to accurate diagnosis

This thesis introduces a novel, non-contact method for assessing the condition of outdoor ceramic insulators by employing an ultrasonic sensor in conjunction with deep learning techniques to detect and classify insulator defects. Notably, it demonstrates how the strong directionality of ultrasonic sensors can be leveraged to indirectly identify internal punctures by monitoring surface discharges on adjacent discs, overcoming attenuation limitations caused by the porcelain body and metallic caps. The dissertation is structured into three phases. In the first phase, ultrasonic data from defective insulator strings is generated under controlled laboratory conditions. A multi-class classification model is developed and trained to diagnose individual defects; the model's performance is then tested in both laboratory and field environments to evaluate its robustness and

real-world applicability. The second phase extends this approach to the diagnosis of insulators with multiple concurrent defects. Here, a multi-label classification model is developed to identify and categorize overlapping defect signatures within a single insulator. This approach captures multiple defect types simultaneously, thereby enhancing diagnostic accuracy and reflecting the true operational conditions of outdoor insulators, where different kinds of degradation can co-exist. The final phase involves in-depth analysis of ultrasonic signals by leveraging model-learned features to identify distinct temporal characteristics for each defect type. This enables precise defect characterization and further boosts the accuracy and reliability of outdoor insulator condition assessment.

Additionally, findings from Shannon entropy analyses corroborate the presence of unique entropy profiles for different defect classes, improving classification performance—though internal puncture and corona classes can exhibit overlapping energy and entropy characteristics. The results highlight the potential for real-time, non-intrusive monitoring, while emphasizing future work on advanced time-frequency analysis and exploring diagnostic methods for polymeric insulators to address broader asset management challenges.

Acknowledgements

First and foremost, I bow in humble gratitude to Allah (SWT), the Most Gracious, the Most Merciful, whose countless blessings, guidance, and mercy have illuminated my path and enabled me to reach this significant milestone in my academic journey. Every step I have taken, every challenge overcome, and every success achieved is solely by His will and infinite grace. His wisdom and provision have sustained me throughout this journey, and I am eternally grateful for the strength, patience, and resilience He has bestowed upon me. Without His divine favor and boundless mercy, none of this would have been possible.

I extend my deepest gratitude to my advisors, Dr. Ayman El-Hag and Dr. Khaled Shaban, for their unwavering support, invaluable mentorship, and steadfast belief in my potential. Your guidance has been instrumental not only in shaping the direction and success of my research but also in fostering my growth as an individual and scholar. Dr. Khaled, your encouragement has inspired me to persevere through challenges and strive for excellence, while Dr. Ayman, your mentorship has gone far beyond the academic realm, providing a sense of reassurance and support that I deeply value. It is rare to find an advisor who provides such profound guidance and support, and I will always cherish the kindness and wisdom you offered during my journey. Your presence, especially during my time in Canada, felt like that of a second father, and I sincerely hope that the bond we have built will extend far beyond my graduation.

To my beloved wife, Sajedah, words cannot fully capture the depth of my gratitude for your endless love, patience, and sacrifices throughout this journey. You have been my anchor during moments of uncertainty and my constant source of motivation. Your faith in me has been a beacon of light, inspiring me to push through even the most difficult times. To my precious daughter, Dina, your laughter and joy have brought warmth and balance to my life, reminding me of the importance of family and the simple pleasures that make life beautiful.

To my beloved parents, Dina and Eyad, your unconditional love, endless prayers, and steadfast belief in me have been the foundation of everything I have accomplished. Your sacrifices, both seen and unseen, are the reasons I stand here today. I owe everything to you,

and there are no words sufficient to express how deeply I appreciate all you have done for me. To my brothers, Ahmad and Hamza, thank you for your encouragement and for always being my biggest supporters.

I am deeply grateful to my colleagues and friends in the High Voltage Lab, particularly Basharat, Safi, and Farouq. Your camaraderie, support, and insightful discussions have been invaluable to my work. The countless hours we spent together navigating challenges and sharing experiences have enriched my academic journey, creating memories that I will cherish forever.

A special note of appreciation goes to my best friend, Al Baraa. Your unwavering support during my transition to Canada was truly a lifeline. From guiding me through new beginnings to countless hours of phone calls, you were always there, offering steadfast friendship and wise counsel when I needed it most. Our conversations filled with laughter, shared memories, and honest reflections on the trials of academia became a sanctuary that kept me grounded throughout this demanding journey. Your kindness and encouragement have been a constant source of strength, and I am profoundly thankful for the pivotal role you have played in my life.

This work would not have been possible without the generous financial support of the Natural Sciences and Engineering Research Council of Canada (NSERC) and the University of Waterloo. Your contributions have alleviated the financial challenges of pursuing higher education, allowing me to focus fully on my research and academic goals.

Finally, I wish to express my heartfelt gratitude to all those who have contributed to this journey, no matter how small their role. Whether through words of encouragement, thoughtful advice, or silent prayers, your support has been invaluable. This thesis is not merely a reflection of my efforts but a testament to the collective support, inspiration, and love that has carried me through. To each of you, I offer my deepest thanks and unending appreciation.

Dedication

To my beloved mother, Dina, and my father, Eyad,
for their endless love, support, and encouragement.

To my dear brothers, Ahmad and Hamza,
for their companionship and unwavering belief in me.

To my beloved wife, Sajedah, and my precious daughter, Dina,
whose love and joy inspire me every day.

Table of Contents

Examining Committee Membership	ii
Author's Declaration.....	iii
Abstract.....	iv
Acknowledgements.....	vi
Dedication.....	viii
List of Figures	xii
List of Tables	xv
List of Abbreviations.....	xvi
List of Symbols.....	xvii
Chapter 1 Introduction	1
1.1 Research Motivation	1
1.2 Outdoor Insulators in Overhead Lines	2
1.2.1 Polymeric Insulators (Composite Insulators)	3
1.2.2 Ceramic Insulators	4
1.3 Mechanisms of Failure in Ceramic Insulators	6
1.3.1 Physical Defects.....	6
1.3.2 Pollution-Related Issues.....	10
1.4 Online Condition Monitoring Techniques.....	11
1.4.1 Binoculars or Standard Cameras	12
1.4.2 Ultra-Violet (UV) Camera.....	12
1.4.3 Infrared (IR) Camera	13
1.4.4 Radio Frequency (RF) Antenna.....	14
1.4.1 Ultrasonic Sensor	15
1.5 Comparison of Non-Intrusive Sensing Techniques.....	16
Chapter 2 Literature Review and Research Gaps.....	18
2.1 Vision-Based Diagnostic Techniques	19
2.2 Radiation-Based Diagnostic Techniques.....	22
2.3 Thesis Objectives and Potential Contributions	25

Chapter 3 Materials and Methods	26
3.1 Multi-Class Classification	26
3.1.1 Experimental Setup	26
3.1.2 Data Collection Using Artificially Introduced Defects	28
3.1.3 Data Preprocessing	32
3.1.4 Multi-Class 1D-Convolutional Neural Network Model	32
3.1.5 Multi-Class Performance Metrics	35
3.1.6 CNN Interpretability using Grad-CAM	37
3.1.7 Laboratory Testing	38
3.1.8 Field Testing	39
3.2 Multi-label Classification	42
3.2.1 Experimental Setup	42
3.2.2 Data Collection using Multiple concurrent defects	43
3.2.3 1-D Convolutional Neural Network for Overlapping Defects	46
3.2.4 Multi-Label Classification Performance Metrics	47
Chapter 4 Results and Discussion	48
4.1 Punctured Disc Detection	48
4.1.1 Configuration 1: A string of two healthy discs	48
4.1.2 Configuration 2: A string of defective disc near the high voltage end	49
4.1.3 Configuration 3: A string of defective disc near the ground end	51
4.1.4 A string of three discs	52
4.2 Multi-Class Classification Results	53
4.2.1 Laboratory Testing Results	53
4.2.2 Field Testing Results	55
4.3 Multi-Label Classification Results	59
4.3.1 Performance Evaluation of the Classification Model	59
4.3.2 Interpretability of CNN Models: Temporal Feature Analysis	61
Chapter 5 Conclusions	68
5.1 Summary and Conclusions	68
5.2 Future Work	69

5.2.1 Enhancing the Current Approach	69
5.2.2 Exploring New Directions	70
References	72
Appendix A List of Papers.....	77

List of Figures

Figure 1.1. Components of an overhead transmission system [8]	3
Figure 1.2 Composite Insulator Sample [9].....	4
Figure 1.3. Typical design of porcelain suspension insulator [2][9].....	5
Figure 1.4 Pin corrosion due to improper stress grading and high contamination [11]	7
Figure 1.5 A radial crack in a ceramic insulator sample due to Portland cement expansion [12]	8
Figure 1.6 Puncture of porcelain dielectric due to a disruptive discharge [9]	9
Figure 1.7 Insulator flashover due to wet contamination.....	11
Figure 1.8 UV camera measurement of a drilled contaminated insulator sample [21]	13
Figure 1.9 DBA on insulator string captured by IR camera	13
Figure 1.10 Overlapping IR and UV images of multiple defects on an insulator string [22].....	14
Figure 3.1 Acoustic measurement setup for detecting various insulator problems in an energized string. a) laboratory setup b) Schematic Diagram	27
Figure 3.2 Hardware Corona generated by a sharp point attached near the HV end of the setup.	30
Figure 3.3 Proposed 1D-CNN Architecture.....	35
Figure 3.4 DBA observed on the ceramic insulator and LBS, highlighted by	39
Figure 3.5 Ultrasonic measurements at different stages:.....	40
Figure 3.6 Loose connection on transformer surge arrester highlighted in red circle.	41
Figure 3.7 Ultrasonic measurement capturing Corona discharges arising from loose connection at transformer surge arrester	42
Figure 3.8 Laboratory experimental setup	43

Figure 3.9 Proposed 1D-CNN Architecture for overlapping defects.....	47
Figure 4.1 1~2 pC of noise observed on the classical PD detector.....	49
Figure 4.2 Image intensifier and acoustic measurements show no signs of surface discharge activities.....	49
Figure 4.3 100 pC of surface discharges observed on the classical PD detector	50
Figure 4.4 Surface discharges predominantly emanating from the healthy disc, as depicted in the image intensifier and acoustic measurement of the insulator string.	50
Figure 4.5 Approximately 50 pC of surface discharges were observed on the classical PD detector.	51
Figure 4.6 Surface discharges persisted on the healthy insulator, as depicted in the image intensifier and acoustic measurement of the insulator string.....	51
Figure 4.7 Approximately 255 pC of surface discharges were observed on the classical PD detector.	52
Figure 4.8 Surface discharges emanating from the healthy insulators, as depicted in the image intensifier and acoustic measurement of the insulator string.....	52
Figure 4.9 Confusion matrix for laboratory testing (Stage 1) (Overall Classification Accuracy: 99.64%).....	54
Figure 4.10 Confusion matrix for laboratory testing (Stage 2).....	54
Figure 4.11 Grad-CAM heatmap of DBA signal on the LBS (15m away).....	57
Figure 4.12 Grad-CAM heatmap of a misclassified DBA signal on the cap-pin insulator (25m away).....	57
Figure 4.13 FFT of the accurately classified vs misclassified DBA signal at the LBS and cap-pin insulator.....	58
Figure 4.14 Confusion matrices for the 20% test split of combined dataset 1 and 2 (Overall Hamming score 98.4%)	60
Figure 4.15 Confusion matrices on dataset 3 (Overall Hamming score 92%).....	60
Figure 4.16 Confusion matrices on dataset 4 (Overall Hamming score 93.2%).....	61
Figure 4.17 Grad-CAM heatmap of healthy insulator signal	62
Figure 4.18 Grad-CAM heatmap of Corona signal.....	62

Figure 4.19 Grad-CAM heatmap of DBA signal	63
Figure 4.20 Grad-CAM heatmap of Punctured Insulator signal	63
Figure 4.21 KDE plot representing the distribution of Shannon entropy across 3,650 ultrasonic signals of all defect types.....	65
Figure 4.22 Ultrasonic signal showing both DBA and corona on an insulator string	66

List of Tables

Table 1. Effectiveness of different non-intrusive sensors for various defects.....	17
Table 2 Omicron MPD 600 Specifications [50]	28
Table 3. Health Condition of the Punctured vs healthy insulators	32
Table 4. Disc Conditions based on Tan and Insulation Resistance Measurement ..	45
Table 5. Summary of Datasets	45
Table 6. Classification Accuracy Across Each Fault Type	55
Table 7. Performance Metric for Each Class Type.....	56
Table 8. Summary of Temporal Features for all Defects.....	67

List of Abbreviations

AC	Alternating Current
RTV	Room Temperature Vulcanizing
ML	Machine Learning
DL	Deep Learning
EPDM	Ethylene Propylene Diene Monomer
DBA	Dry Band Arcing
HVEL	High Voltage Engineering Laboratory
ESDD	Equivalent Salt Deposit Density
NSDD	Non-soluble Deposit Density
IR	Infra-Red
UV	Ultra-Violet
PD	Partial Discharge
RF	Radio Frequency
AI	Artificial Intelligence
UAV	Unmanned Aerial Vehicles
ROW	Rolling on Wire
ANN	Artificial Neural Networks
R-CNN	Region-based Fully Convolutional Networks
YOLO	You Only Look Once
SSD	Single Shot Multi-Box Detector
PNN	Probabilistic Neural Network
SSA	Sparrow Search Algorithm
KPCA	Kernel Principal Component Analysis
RH	Relative Humidity
CNN	Convolutional Neural Network
Grad-CAM	Gradient-weighted Class Activation Mapping
ReLU	Rectified Linear Unit
LBS	Load Break Switch
FFT	Fast Fourier Transform
KDE	Kernel Density Estimation
STFT	Short-Time Fourier Transform
WT	Wavelet Transform
EMD	Empirical Mode Decomposition

List of Symbols

Z	Normalized Value (Z-score)
μ	Mean of the data set
σ	Standard Deviation of the dataset
x_{i+j-i}	input at position $i+j-1$
$w_j^{(k)}$	weight of the k -th filter (kernel) at position j
$b^{(k)}$	bias of the k -th filter.
σ	activation function (e.g., ReLU, $\sigma(z) = \max(0, z)$)
M	kernel size
$y_i^{(k)}$	feature map value at position i for the k -th filter after applying the convolution operation
P	Probability
Z_C	Raw score of class
Z_k	raw score of all classes $k = 1, 2, 3, \dots, C$
C	Total Number of Classes
\mathcal{L}	Cross-entropy loss function
$y_{i,c}$	True label for sample for class c for sample i
$\hat{y}_{i,c}$	Predicted probability for class c for sample i
TP	True Positive
TN	True Negative
FP	False Positive
FN	False Negative
Grad	Gradient
y^c	Predicted class score for class c
k	Number of feature maps
A^k	k th feature map
Z	Length of one feature map
α_k^c	Average gradients for class c
$L_{\text{Grad-CAM}}^c$	Grad-CAM heat map
N	Total number of instances
i	Instance

y_i	True labels for instance i
\hat{y}_i	Predicted labels for instance i
\cup	Union
\cap	Intersection
H	Shannon Entropy
N	Total number of unique intensity levels in the signal
p_i	Probability of occurrence of the i-th intensity level
n_i	count of occurrences of the i-th intensity level in the signal
$\sum_{j=1}^{\omega} n_j$	Total number of samples in the signal

Chapter 1

Introduction

1.1 Research Motivation

Outdoor insulators are crucial components in overhead transmission and distribution lines. Although they represent only 5-8% of the total capital cost of transmission lines, they account for more than 70% of power line outages and 50% of maintenance costs [1]. Consequently, the continuous diagnostics of these assets is essential for mitigating premature failure risks.

It is estimated that approximately 150 million ceramic insulators are currently deployed in North American overhead transmission and distribution networks [2]. Many of these insulators have either approached or exceeded their intended lifetime. While some continue to operate satisfactorily, others show serious signs of aging, which may lead to complete failure. As a result, utilities are increasingly concerned about assessing the condition of these aging assets and taking corresponding actions accordingly. These actions include implementing regular washing regimens for insulators, applying/re-applying room temperature vulcanizing (RTV) coatings, or, in the worst-case scenarios, developing replacement strategies for defective insulators.

Non-intrusive condition monitoring techniques are preferred for field inspections, as they allow online assessments without the need to remove insulators from service. However, these methods often depend on the operator's experience and subjective judgment, making the process time-consuming and prone to inaccuracies in data interpretation. Compounding these challenges is the decline in available expertise for outdoor insulator inspection in recent years, underscoring the need for intelligent systems that can supplement the reduced skilled workforce, automate inspection procedures, and enhance monitoring efficiency. Achieving these objectives requires effective non-intrusive sensing and measurement techniques, coupled with advanced signal processing and machine learning tools [3, 4].

Recently, machine learning has advanced significantly with the advent of deep learning, which has demonstrated superior accuracy and robustness in various applications. Over

the past decade, a growing body of research has leveraged deep learning models for assessing the condition of outdoor insulators [5-6]. One key advantage of deep learning over traditional machine learning algorithms is its ability to incorporate feature extraction within the learning process, thus reducing the need for extensive data preprocessing. However, deep learning models require large volumes of training data, which can sometimes be difficult to obtain. Data augmentation techniques can help by expanding existing datasets to generate additional training samples [7].

This introductory chapter provides an overview of outdoor insulators, focusing specifically on ceramic insulators and their failure mechanisms. It also examines the online condition monitoring techniques commonly used in the industry.

1.2 Outdoor Insulators in Overhead Lines

AC power can be transmitted and distributed through either underground cables or overhead lines. Although underground cables are often preferred in urban networks for their aesthetic appeal, they involve significantly higher installation costs. As a result, overhead lines are widely adopted in transmission systems and rural distribution networks, where cost-effectiveness is crucial.

Overhead transmission systems generally consist of three primary components: conductors, insulators, and tower structures. The tower structure and insulator design vary based on the system's voltage level. Figure 1.1 illustrates the design of a high-voltage transmission tower in the 132–220 kV range. Insulators provide mechanical support to high-voltage conductors while electrically insulating them from the grounded tower structure. Two primary types of insulators are currently used in the industry: ceramic (porcelain and glass) and non-ceramic polymeric insulators (such as EPDM, epoxy, and silicone rubber). Although ceramic insulators have been gradually replaced by polymeric ones over the past few decades, they remain in use in modern electric grids. Among ceramic insulators, glass types are preferred by many utilities because their visual inspection leaves no ambiguity, as they either remain intact or shatter completely. The following sections offer an overview of both types and compare their key characteristics.

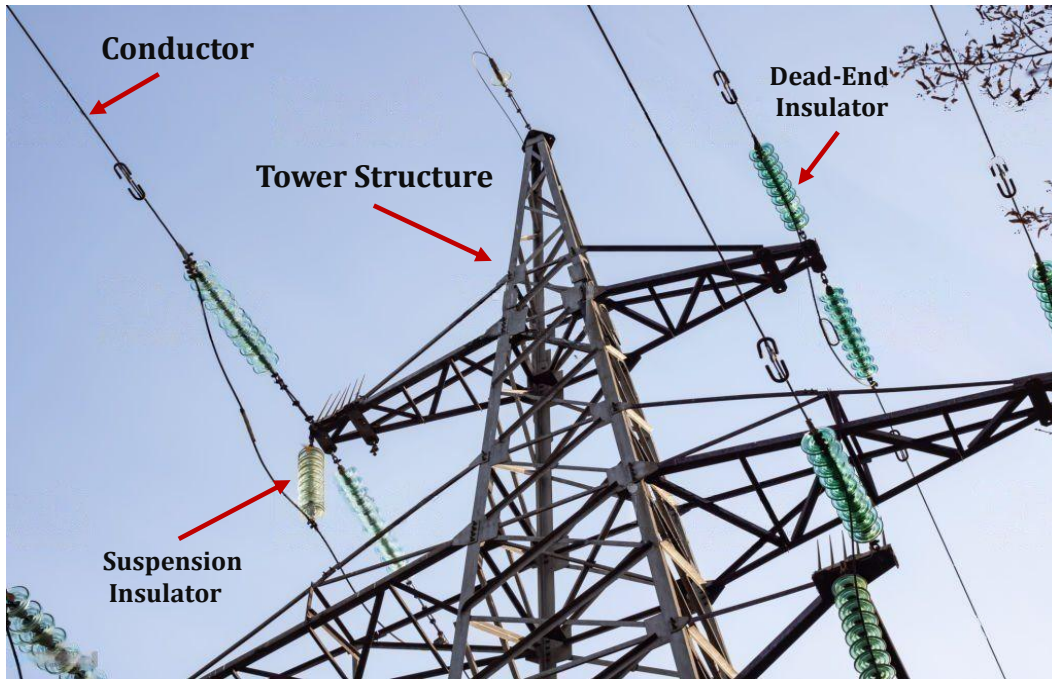


Figure 1.1. Components of an overhead transmission system [8]

1.2.1 Polymeric Insulators (Composite Insulators)

Polymeric insulators, also referred to as composite insulators, consist primarily of a fiberglass core rod surrounded by a housing material (Figure 1.2). The fiberglass rod provides the necessary mechanical strength to support the weight of overhead conductors, while the housing—commonly silicone rubber—supplies the essential insulating properties.

In recent years, polymeric insulators have dominated the insulator market due to several advantages over traditional ceramic insulators. These advantages include lighter weight, hydrophobic properties, and strong resistance to vandalism. These features not only make polymeric insulators easier to handle but also ensure superior performance in heavily contaminated or wet environments.

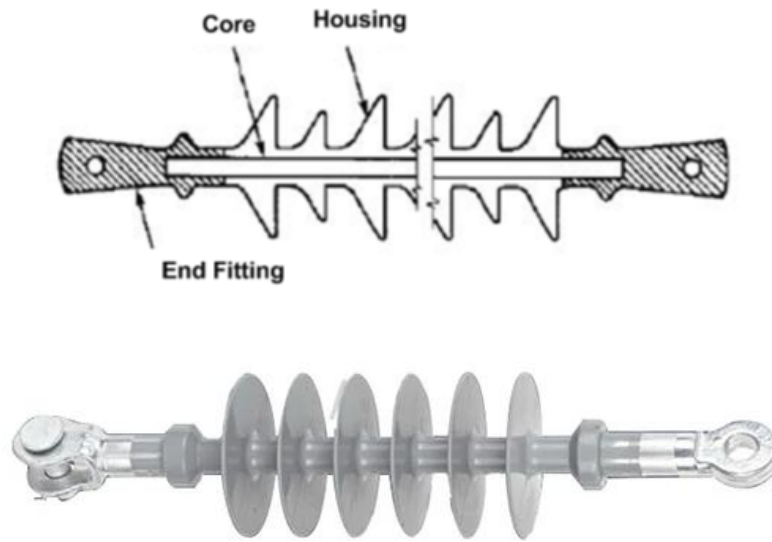


Figure 1.2 Composite Insulator Sample [9]

Despite these benefits, polymeric insulators are susceptible to aging when exposed to harsh environmental conditions such as high temperatures, humidity, and UV radiation. Moreover, corona discharges can produce nitric acid, which degrades the housing material. Dry band arcing (DBA) may also lead to tracking and erosion, potentially causing mechanical failure. Given that polymeric insulators are relatively new, their long-term reliability remains uncertain, emphasizing the need for continued research to improve their performance under various environmental conditions.

1.2.2 Ceramic Insulators

Ceramic insulators, introduced in the early 1900s, have undergone multiple developments in shell profiles and hardware designs. They consist mainly of a porcelain-fired dielectric shell, coated with a glaze that seals the surface and enhances its mechanical strength. Galvanized metal end fittings—often with flexible bituminous coating—from the cap and pin, which allow the insulator to bear mechanical conductor loads. Cement is used to bond the dielectric shell to the metallic hardware. Figure 1.3 shows a typical suspension-type porcelain insulator. Depending on the applied voltage and pollution severity, a series of ceramic discs is connected in string form, each disc potentially made from porcelain or glass.

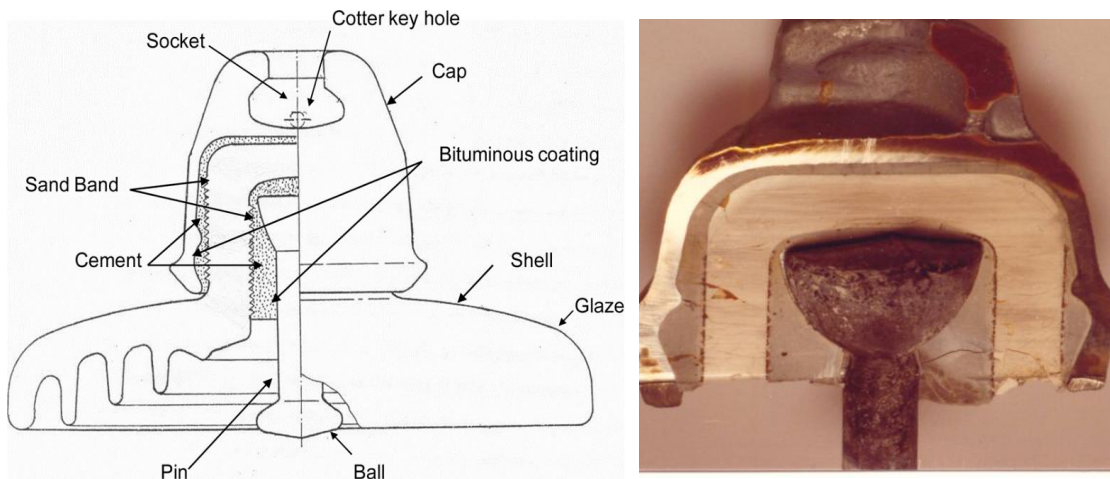


Figure 1.3. Typical design of porcelain suspension insulator [2][9]

Ceramic insulators offer advantages such as chemical stability, high resistance to erosion and tracking, and a relatively uniform electric field distribution compared to polymeric insulators. This smoother field distribution is largely due to the cap-and-pin configuration, in which each disc acts as a capacitor with a fixed voltage, creating a graded voltage profile from high voltage to ground [10]. Consequently, stress grading rings are often unnecessary—although at very high voltage levels, this may not hold true.

On the downside, ceramic insulators are heavy and exhibit brittle characteristics. Therefore, it is imperative to implement specialized measures during their handling and transportation to minimize the risk of breakage. Furthermore, ceramic insulators are considered appealing targets for vandals and are vulnerable to damage from external impacts, such as gunfire.

Another significant drawback is their hydrophilic surface, which form water films under wet conditions. When conductive pollution accumulates on these wet surfaces, the resulting drop in surface resistance can allow leakage currents to flow, potentially leading to DBA and flashover. As a result, ceramic insulators require regular washing, increasing their maintenance costs compared to polymeric alternatives.

Ceramic insulators are designed to endure weathering and aging; however, like all materials, they inevitably deteriorate over time. This aging process is often accelerated by environmental factors such as extreme weather conditions, physical damage, pollution, and

corrosion. With the electrical grid comprising numerous aging and defective ceramic insulators, the work conducted for this thesis will be solely focused on ceramic insulator diagnostics. The following section offers a comprehensive analysis of the failure mechanisms of ceramic insulators, providing critical context for the development and application of diagnostic methods.

1.3 Mechanisms of Failure in Ceramic Insulators

Assessing insulator failures is challenging due to the complex interplay of electrical, mechanical, and environmental stresses. While some defects are readily visible, others remain hidden and require sophisticated diagnostic tools for detection. Failures may stem from physical defects or pollution-related factors. This section highlights key aging mechanisms and the ultimate failure modes of ceramic insulators.

1.3.1 Physical Defects

1.3.1.1 Pin Corrosion

Pin corrosion commonly occurs in insulators exposed to high contamination levels and inadequate stress grading. At higher voltages, poor stress grading can initiate corona discharges, which gradually erode the protective galvanized layer and render the cap susceptible to corrosion. Additionally, inadequate galvanization and the absence of cathodic protection further accelerate pin degradation. When leakage currents flow on a wet, contaminated insulator surface, electrolytic corrosion can develop, substantially reducing the pin's cross-sectional area and mechanical strength, as shown in Figure 1.4. The rate of pin corrosion also varies between insulator types, with dead-end insulators experiencing higher exposure and faster deterioration compared to suspension insulators, where the pin remains more sheltered. Without timely intervention, this degradation may compromise the insulator's ability to support the conductor, potentially causing the conductor to drop.



Figure 1.4 Pin corrosion due to improper stress grading and high contamination [11]

1.3.1.2 Radial Cracking

Portland cement is widely used in assembling porcelain suspension insulators. Field evidence indicates that over extended service periods, the dielectric shells of some porcelain insulators may develop radial cracking due to expansion of the Portland cement that binds the insulator structure. Ceramic insulators, being brittle, are particularly susceptible to cracking under the stress caused by the expanding cement. Moist atmospheric conditions—rain or high humidity—further accelerate cement expansion. Newer ceramic insulator designs integrate a bituminous layer to counteract cracking, but this layer deteriorates over time, causing uneven stress distribution that can lead to cracks in the dielectric shell. Figure 1.5 illustrates a radial crack resulting from the expansion of Portland cement, along with the gradual aging effects on the bituminous layer.



Figure 1.5 A radial crack in a ceramic insulator sample due to Portland cement expansion [12]

1.3.1.3 Internal Punctures

Outdoor insulators are frequently exposed to surge impulse voltages caused by lightning strikes or switching events. Lightning impulses, in particular, can exhibit rise times with steepness reaching several thousand kilovolts per microsecond [2]. While sound insulators are designed to endure such stresses, the presence of impurities or large voids near the shell, especially in poorly manufactured insulators, significantly increases the likelihood of punctures. Additionally, moisture ingress can lead to cement growth, further exacerbating the risk of puncture formation.

Punctured insulator units often appear mechanically intact and continue to bear mechanical loads; however, they lose their ability to support the disc's full rated voltage. Even a single punctured unit can compromise the mechanical integrity of the entire string, particularly during flashover events. Following a flashover, the resulting power-follow current — which can reach substantial magnitudes — is directed along a path determined by the internal and external impedances of the insulator. Punctured units, having lower internal impedance than intact ones, allow a considerable portion of this current to pass through the disc. The resulting forces can lead to severe damage, causing the porcelain to detach from the cap and, in extreme cases, resulting in the conductor's failure and drop.

Figure 1.6 presents a cross-sectional view of a dissected ceramic insulator disc with a visible punctured pathway formed by a disruptive discharge. Such punctures not only result in a permanent reduction in insulation strength but also impose additional stress on neighboring insulators, accelerating their aging process.

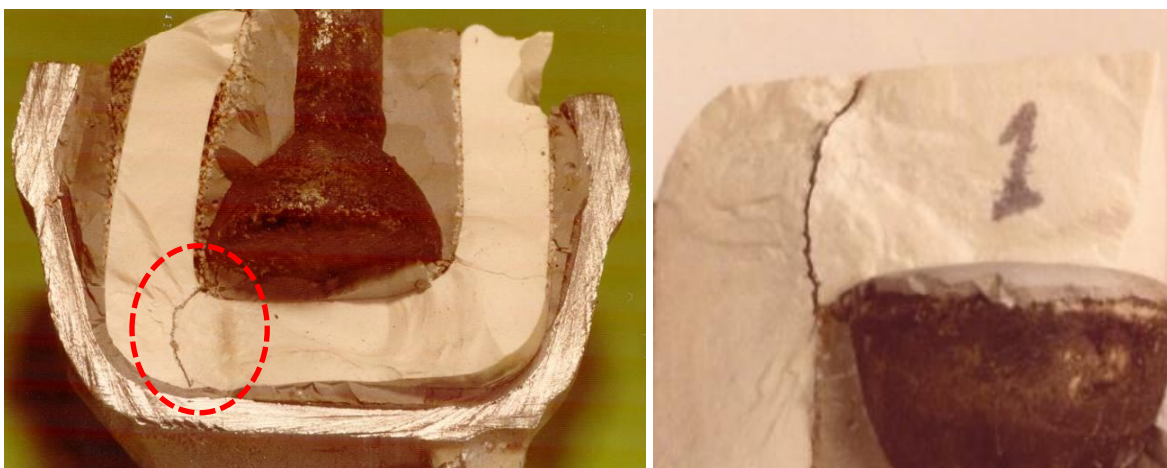


Figure 1.6 Puncture of porcelain dielectric due to a disruptive discharge [9]

Punctured discs can be detected using offline testing methods, such as the AC flashover test. A significant reduction in the flashover voltage, compared to the typical 80-90 kV for intact discs, often indicates the presence of a partially punctured unit.

In addition to offline methods, several non-intrusive techniques are available for identifying defective insulators, including the buzz test and the ping test. The buzz test relies on the potential difference across successive discs in an energized insulator string. During the buzz test, an inspection rod with two metal prongs is applied across each disc. If the insulator is intact, the potential difference will be sufficient to cause a dielectric breakdown in the air, producing a distinctive buzzing sound. Conversely, a defective disc with reduced voltage withstand capability will generate no sound due to lack of adequate potential difference.

While the buzz test is effective, it is both time-consuming and labor-intensive, requiring linemen to climb transmission towers to conduct the assessment. Despite comprehensive safety training and strict procedures to mitigate hazards, working at heights near energized HV conductors remains inherently risky.

The ping test on the other hand provides another non-intrusive detection method by evaluating the acoustic response of the porcelain shell when struck with a hard object. An intact insulator typically produces a clear, ringing sound with a long sustain, whereas a defective one emits a dull, muffled sound, often indicative of a fracture. Although the ping test is simple and cost-effective, its accuracy largely depends on the operator's experience in interpreting the sound, making it both subjective and time-consuming.

1.3.2 Pollution-Related Issues

Dust, sand, volcanic ash, and salt from coastal regions can accumulate on insulator surfaces. When these contaminants become wet — due to fog, dew, or high humidity — the risk of flashover increases substantially. This issue is particularly critical for ceramic insulators, which are hydrophilic. As a result, their surface resistance decreases, allowing leakage currents to flow. The heat generated by these currents dries certain regions of the insulator's surface, leading to the formation of dry bands. Since these dry bands exhibit higher resistance compared to the wet areas, localized voltage stress develops, which can initiate DBA.

As the wetting process continues, the discharge current intensifies, causing the arcs to elongate and propagate. Eventually, the discharge may bridge the insulator, leading to a complete flashover [13]. Figure 1.7 illustrates a flashover event on a string of two porcelain insulators heavily coated with wet pollutants.

In addition to contamination, frost accumulation presents further challenges for insulator performance. Unlike water, ice is non-conductive at temperatures below 0°C. However, as the temperature rises and approaches the freezing point, ice can become conductive due to the formation of a thin liquid layer on its surface. This effect is particularly pronounced during the spring when melting occurs. The presence of salts, often originating from coastal environments or road de-icing operations, can further enhance the conductivity of this liquid layer by forming an electrolyte. As a result, leakage currents increase, leading to dry band formation and subsequent arcing. The resulting positive feedback mechanism exacerbates DBA, significantly increasing the potential risk of flashovers.

Consequently, frost-related DBA remains a major concern in regions experiencing seasonal freeze-thaw cycles.



Figure 1.7 Insulator flashover due to wet contamination

Although ceramic insulators are designed to withstand flashovers, such events can cause power outages and affect the reliability of the power grid. Utilities therefore monitor pollution severity, commonly through equivalent salt deposit density (ESDD) and the non-soluble deposit density (NSDD), to plan effective washing schedules.

1.4 Online Condition Monitoring Techniques

Regular condition monitoring and diagnostics are essential for averting premature insulator failures and sustaining power system reliability. As utilities strive to meet the growing demand for uninterrupted power delivery, adopting effective diagnostic techniques becomes increasingly important. Traditional intrusive methods require de-energizing lines and removing insulators from service, posing major drawbacks in reliability, safety, time, and cost. Consequently, online diagnostic techniques are generally preferred for field inspections because they offer a faster, safer, and more reliable alternative.

This section explores the online diagnostic techniques currently used in the field, broadly classified into vision-based and radiation-based methods.

Vision-based techniques involve sensors such as infrared (IR) [14-15], ultraviolet (UV) [16-17], and standard cameras [18-19], which can detect defects including broken discs, corona, and temperature anomalies linked to DBA or PD. Radiation-based methods use ultrasonic sensors or radio frequency (RF) antennas to detect the ultrasonic and electromagnetic emissions from defective insulators. Each method has unique advantages and limitations, as outlined in the subsections below.

1.4.1 Binoculars or Standard Cameras

Visual inspection using cameras provides a quick, cost-effective way to detect obvious external defects, such as severe corrosion, broken shells, missing discs, or large cracks. Skilled operators typically use high-powered binoculars during routine line patrols. While widely adopted by utilities, this method cannot reliably detect certain flaws, especially those located in hard-to-visualize areas or within the insulator's internal structure. As a result, it is mostly used for preliminary assessments, with more advanced methods required for comprehensive diagnostics.

1.4.2 Ultra-Violet (UV) Camera

PD activity serves as a reliable early indicator of defective insulators. Cracked discs emit surface PD, which generates UV radiation within the 300-400 nm wavelength range—undetectable by the human eye or standard light-intensifying tools. Consequently, UV cameras, commonly known as corona cameras, are essential for detecting cracks in the dielectric shell. These cameras are also particularly effective in identifying hardware-related issues, such as corona discharges from protrusions and defective end fittings. Furthermore, they play a vital role in assessing contamination severity by visualizing DBA activity [20]. Figure 1.8 presents a UV measurement of a drilled, contaminated ceramic insulator. While corona cameras excel in detecting external discharges caused by cracks, wet contamination, or other surface defects, they are incapable of identifying internal defects that do not emit UV radiation to the surface.



Figure 1.8 UV camera measurement of a drilled contaminated insulator sample [21]

1.4.3 Infrared (IR) Camera

IR imaging is widely considered the standard technique for identifying defects linked to temperature rises, such as DBA. It is particularly adept at detecting joule heating caused by leakage currents on wet, contaminated insulator surfaces. Figure 1.9 illustrates DBA activity recorded via IR imaging on a string of wet, contaminated porcelain insulators in the High Voltage Engineering Laboratory (HVEL).

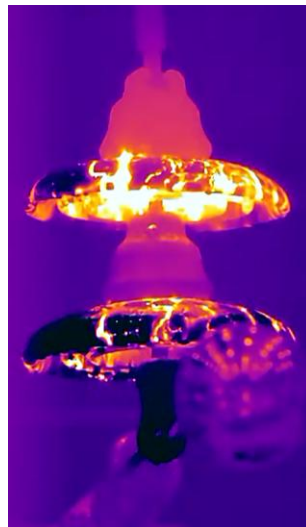


Figure 1.9 DBA on insulator string captured by IR camera

In some cases, IR imaging can detect PD in later stages or reveal insulator punctures associated with significant internal arcing. Nevertheless, IR is generally less reliable than UV imaging for identifying PD, as PD often generates less heat in its early stages. Consequently, IR and UV cameras are frequently used together in the field, providing a more comprehensive assessment. Figure 1.10 presents an overlapping IR and UV image showing multiple defects on the same insulator string [22]. The white spot corresponds to corona discharges from sharp points on the metallic hardware, while the orange spots indicate localized heating that may signal internal defects. The combined IR and UV data thus offer complementary diagnostic insights.



Figure 1.10 Overlapping IR and UV images of multiple defects on an insulator string [22]

1.4.4 Radio Frequency (RF) Antenna

PDs in defective insulators emit high-frequency electromagnetic waves ranging from hundreds of MHz to several GHz, which can be detected using RF antennas tuned to the appropriate bandwidth. The emission frequency varies with the defect type; for instance, internal voids typically generate higher-frequency signals in the GHz range, while surface discharges and corona predominantly produce signals in the MHz range [23]. These frequency differences can serve as valuable features for classifying defect types.

A key strength of RF antennas is their sensitivity to these frequency variations, enabling effective defect classification. However, their field deployment faces challenges, including interference from communication signals. To mitigate this, RF antenna designs must incorporate frequency filtering, shielding, or adaptive signal processing to maintain sensitivity to PD emissions. Despite these advantages, the practical application of RF antennas in online condition monitoring is limited by the need for bulky, specialized equipment such as oscilloscopes and data acquisition systems, making them less suitable for continuous diagnostics of outdoor insulators.

1.4.1 Ultrasonic Sensor

Ultrasonic sensors have become a reliable, cost-effective option for condition monitoring of outdoor insulators. PDs occurring in defective insulators generate ultrasonic signals with frequencies exceeding 20 kHz. Although these signals are inaudible to the human ear, they can be effectively captured using parabolic-dish ultrasonic sensors equipped with highly sensitive microphones and high-gain filters [24]. The directional characteristics of these sensors enable them to focus on specific sound sources while minimizing ambient noise interference.

A notable advantage of ultrasonic sensing is its ability to detect a broad range of defect signatures, including high-frequency discharges such as PDs and low-frequency discharges like DBA. Unlike RF antennas—which require bulky, specialized equipment—ultrasonic sensors are compact, user-friendly, and better suited for online inspections. They are also immune to electromagnetic interference and are more cost-effective, as they do not need extensive data acquisition systems.

However, the current effectiveness of ultrasonic sensing largely depends on operator expertise, which can introduce subjectivity into the diagnostic process. To address this limitation, researchers are increasingly integrating AI to automate data processing, aiming to improve diagnostic accuracy, consistency, and overall efficiency.

1.5 Comparison of Non-Intrusive Sensing Techniques

Non-intrusive sensing approaches offer a variety of mechanisms for detecting defects in high-voltage ceramic insulators, with each sensor relying on a distinct detection principle tailored to specific defect characteristics. For example, PD caused by an external crack may generate ultrasonic emissions, electromagnetic waves, ultraviolet light, or, in advanced stages, heat. These phenomena can be detected using ultrasonic sensors, RF antennas, UV cameras, or IR cameras, respectively. Additionally, if the crack is visible, it can be identified using a standard optical camera.

Punctured porcelain insulator discs provide a clear demonstration of how various sensors excel at detecting different stages of defect progression. In the early stages, internal PD activity is most effectively captured by RF antennas, which are sensitive to high-frequency electromagnetic emissions originating within the dielectric material. As the defect advances, surface PD may develop on nearby healthy discs. This surface activity is detectable by UV cameras or ultrasonic sensors, both of which provide valuable spatial and temporal insights into the discharge, aiding in the identification of the punctured disc. In later stages, as internal PD intensifies and transitions into severe arcing, IR cameras can reliably detect the resulting heat signature, enabling precise defect localization. This multi-stage detection process highlights how integrating multiple sensing techniques enhances diagnostic accuracy by leveraging their complementary strengths.

The performance of any given sensor is influenced by factors such as the severity of the defect, the distance between the sensor and the insulator, and the level of surface contamination. Table 1 summarizes the capabilities of various sensors in detecting ceramic insulator defects, offering a comprehensive view of their diagnostic effectiveness.

Among the available sensor types, RF antennas and ultrasonic sensors exhibit the widest range of remote defect detection capabilities. However, ultrasonic sensors are typically preferred for field inspections due to their compact design, cost-effectiveness, and immunity to electromagnetic interference. In practice, multiple sensors are often deployed in combination to obtain complementary data. For example, pairing IR and UV cameras or integrating ultrasonic sensors with optical cameras (e.g., acoustic cameras) can significantly

improve diagnostic precision. A detailed comparative analysis of these sensors is provided in [25].

Table 1. Effectiveness of different non-intrusive sensors for various defects

Serial No.	Problem	Non-intrusive sensors				
		Vision Based			Radiation Based	
		Regular Camera	IR Camera	UV Camera	Ultrasonic sensor	RF Antenna
1	Broken disc	•••				
2	Corrosion of hardware	•••				
3	Hardware Corona	•	•	•••	•••	•••
4	Punctured Discs		•		••	•••
5	External Cracks	••	•	••	••	••
6	Wet Contamination	•	•••	•••	•••	••

Chapter 2

Literature Review and Research Gaps

One commonly employed practice in insulator diagnostics is the use of crewed helicopters equipped with sensors such as IR, UV, and optical cameras to collect inspection data [26]. While this method has an excellent safety record due to the high level of crew training and stringent operational protocols, it remains costly. The expenses associated with maintaining helicopters, employing specialized personnel, and ensuring regulatory compliance contribute to the overall operational cost. To address these financial challenges, alternatives such as unmanned aerial vehicles (UAVs) [27] and Rolling on Wire (ROW) robots [28] have been proposed. However, these emerging technologies have yet to demonstrate significant cost savings, making further advancements in autonomous inspection and operational efficiency essential for their wider adoption.

The extensive data gathered through these inspections is typically analyzed manually by experienced personnel—a process that not only slows down maintenance but also increases operational costs. Automating this procedure through trained machine learning models offers a promising solution, enabling faster and more accurate diagnoses.

Previous studies have applied machine learning techniques, such as Artificial Neural Networks (ANNs), to classify defects in ceramic insulators [24][29]. While these models have demonstrated some effectiveness, they often struggle to capture complex, non-linear relationships within the data and rely heavily on manual feature engineering. In contrast, deep learning algorithms learn hierarchical representations directly from raw data, thereby reducing the need for extensive feature extraction. Additionally, robust pre-trained models—developed using high-performance computing resources—have significantly expanded the utility of deep learning approaches, consistently leading to more accurate and reliable diagnostic outcomes.

This chapter reviews non-intrusive diagnostic methods that employ machine learning and deep learning to assess the condition of ceramic insulators. Existing literature can be broadly categorized into two primary domains: (1) vision-based diagnostic techniques (2)

radiation-based diagnostic techniques. Both approaches primarily use image processing, computer vision, and signal processing to extract features for classification tasks. The following sections provide an in-depth review of each domain, emphasizing recent advancements and emerging trends.

2.1 Vision-Based Diagnostic Techniques

Vision-based techniques, utilizing IR, UV, and standard cameras, are effective in detecting defects such as cracks, corona, and temperature anomalies associated with DBA or severe PD. However, these sensors are often limited to pinpointing defect locations without identifying their underlying causes. For example, although UV cameras can capture surface discharges, they cannot distinguish whether the source is a crack or wet contamination. Consequently, integrating complementary sensor technologies is essential for accurate root cause diagnosis.

Researchers have mainly used image processing with standard cameras to identify external physical defects, including cracks, missing discs, and broken discs in ceramic insulator strings. Most proposed approaches adopt deep learning algorithms, following a common workflow: (1) the insulator is first localized in the image using object detection. (2) a trained deep neural network then classifies the localized region to determine the specific defect.

Deep learning algorithms for object detection generally fall into two categories: two-stage networks and one-stage networks [30]. Two-stage networks (e.g., Regions with Convolutional Neural Networks (R-CNN), Fast R-CNN, Region-based Fully Convolutional Networks (R-FCN), and Mask R-CNN) first generate regions of interest and then classify the extracted features, often achieving higher detection accuracy but at the cost of slower inference speeds. One-stage networks (e.g., You Only Look Once (YOLO) and Single Shot Multi-Box Detector (SSD)) are end-to-end models that simultaneously predict positional information and classification probabilities, offering faster inference. These models prioritize speed, making them well-suited for real-time and time-sensitive applications.

An example of a two-stage network is proposed in [31], featuring a deep CNN cascaded architecture. The first network detects insulators by drawing bounding boxes around them

and cropping up these regions, while the second network identifies missing discs within the cropped images. Data augmentation was applied to address the scarcity of defective images for training. The system achieved precision and recall values of 91% and 96%, respectively.

To enhance detection speed, [32] proposed a one-stage network based on YOLOv3 for classifying broken ceramic insulator discs. To address the issue of blurry aerial images, the authors integrated a super-resolution CNN to upscale images prior to classification. This approach achieved both high speed and impressive accuracy, with a classification accuracy of 95.6% for insulator defect detection. However, despite their high classification performance, these models rely on powerful computing platforms with substantial resources, rendering them unsuitable for onboard CPU systems in drones, which operate under strict hardware constraints. Additionally, these models remain untested on edge devices like Raspberry Pi, which possess significantly limited computational capabilities.

Large deep-learning models generally require extensive computational resources, resulting in slower classification speeds and straining the processing capacities of edge devices. To overcome these challenges, [33] and [34] introduced drone-based inspection systems for power line ceramic insulators using edge devices. By striking a balance between computational efficiency and performance, these systems facilitate reliable and rapid defect detection in resource-constrained environments. The authors considered four insulator conditions: healthy, broken discs, contamination, and defective surfaces. An object detection model was trained on 6,020 insulator images—augmented to reduce overfitting—and deployed on a hexacopter equipped with a camera and a Raspberry Pi 4. YOLOv8n model achieved a mAP@50 of 99.4% and an inference time of just 2.08 seconds, outperforming other single-stage object detectors, largely due to its advanced transformer-based architecture.

Vision-based techniques have also been explored for estimating pollution levels on insulator surfaces. Pollution severity are typically quantified by ESDD and NSDD. Traditionally, determining these parameters requires a power shutdown and the removal of insulator samples from the field for laboratory analysis. This process involves collecting and weighing contamination from the insulator surface and calculating the ESDD/NSDD

values in mg/cm^2 . [35][36]. While accurate, this approach is time-consuming, intrusive, and operationally inefficient.

To minimize power shutdowns, various online techniques have been proposed for pollution-level assessment, including those based on image processing. In [37], standard optical cameras and image processing were used to estimate NSDD levels. Insulators were first isolated in each image, and then a grayscale histogram was employed to track changes in pixel intensity corresponding to pollution deposits. An increase in white-colored pollutants resulted in a higher frequency of white pixels in the histogram. Features such as relative area and the global mean of the first 80 tonal values were extracted then fed into a neural network, which achieved a classification accuracy of 93.75% for categorizing NSDD levels into low, medium, and high. Despite its high accuracy, this method did not account for variations in the color and composition of non-soluble deposits across different geographical regions and environmental conditions, highlighting the need for more adaptable and robust approaches.

ESDD estimation has similarly been explored using infrared and ultraviolet imaging. For instance, [38] demonstrated that higher ESDD and humidity levels lead to more pronounced heating, wider temperature ranges, and more dispersed temperature distributions in IR images. A Probabilistic Neural Network (PNN) was built to map these IR features—along with ambient temperature and humidity—to pollution levels. Optimized with Sparrow Search Algorithm (SSA) and Tent chaotic mapping, the model achieved 86.5% accuracy.

In [39], UV imaging was utilized to estimate ESDD levels. Insulators were uniformly contaminated to ESDD values of 0.1, 0.2, and 0.4 mg/cm^2 . Discharge activity was recorded using a UV camera under a specific applied voltage, and the captured images were preprocessed into binary formats to highlight the discharge regions. These binary images were then analyzed using a CNN, which classified pollution severity with an average accuracy of 85%.

To enhance classification accuracy, [40] introduced a hybrid approach that combined IR and UV imaging. Contamination was applied to insulators in accordance with IEC 60507 standards, and features were extracted from both imaging modalities. These extracted features were fused using the Fisher criterion for feature selection and kernel principal

component analysis (KPCA) for dimensionality reduction, before being fed into an ANN. This integrated method achieved an overall accuracy of 96.67%, significantly outperforming the individual accuracies of IR imaging (81.67%) and UV imaging (75.83%).

Despite these advancements, factors such as ambient temperature, solar radiation, and heat dissipation significantly affect surface temperature, making IR imaging less reliable for pollution-level estimation under certain environmental conditions. Although combining IR and UV data can improve diagnostic accuracy, the method's effectiveness is highly dependent on sufficient relative humidity to facilitate surface discharges. However, under dry ambient conditions, this diagnostic approach becomes less effective, limiting its capability to accurately estimate pollution levels.

Addressing this constraint, [41] proposed a method that combines both visible-light images and IR information to estimate pollution severity. Visible-light imaging is applied for relative humidity (RH) below 60%, and incorporates IR information for corrections when RH exceeds 60%. A mathematical model relates ESDD levels to color features, yielding classification accuracies of 84% at $RH < 60\%$ and 89% at $RH \geq 60\%$. Although the approach accounts for variable environmental conditions, its accuracy remains relatively modest. These methods, while potentially useful for preliminary assessments in controlled scenarios, are inherently non-calibrated and may not accurately quantify pollution in every real-world setting.

2.2 Radiation-Based Diagnostic Techniques

Although vision-based methods excel at identifying and locating external defects, they are less effective in detecting internal defects. To address this limitation, radiation-based techniques, such as those utilizing RF antennas and ultrasonic sensors, have become valuable diagnostic tools. These sensors can capture distinct signals emitted by different types of defects, providing data that is particularly suitable for analysis using machine learning or deep learning models [42–44].

For instance, in [45], the classification of various defect types in ceramic insulators was performed by analyzing electromagnetic signals obtained through RF antennas. The study specifically examined three defect types: cracked insulators, insulators with a hole through

the cap, and fully broken insulators. Wavelet features were extracted from the measured signals and used as input for a neural network. The laboratory tests achieved a classification accuracy of 97%, although this accuracy decreased to 91% under field conditions. Despite these promising results, the study's applicability in real-world scenarios is somewhat limited, as only two defect types (cracked and broken insulators) were considered during the field tests.

Wideband RF antennas are especially effective in detecting corona discharges (in the MHz range) and internal defects (in the GHz range). However, their broad bandwidth makes them susceptible to noise and electromagnetic interference. Although some antenna designs incorporate band-reject features to reduce interference, designing an antenna that spans such a wide frequency range remains a formidable challenge. Moreover, RF antennas require bulky equipment such as oscilloscopes and specialized data acquisition systems, reducing their feasibility for real-time, online monitoring of outdoor insulators.

By contrast, ultrasonic sensors show significant promise for outdoor insulator diagnostics. They are immune to electromagnetic interference and exhibit strong directionality, which minimizes the impact of ambient noise. Additionally, they can detect a wide range of defects—ranging from high-frequency phenomena like PD to lower-frequency activities such as DBA—while being more cost-effective than RF antennas or UV cameras. However, traditional ultrasonic diagnostics often hinge on operator expertise, leading to subjective evaluations that can affect consistency and efficiency. Thus, Integrating AI-driven analytics offers a promising solution for achieving more accurate, objective, and rapid ultrasonic diagnostics.

Recent studies have integrated ultrasonic sensors with machine learning and deep learning techniques to enhance insulator diagnostics. For example, in [44] and [46], neural networks were employed alongside ultrasonic measurements in both controlled samples and string configurations. In [46], frequency-dependent features extracted from the acoustic signal envelope were used to train an artificial neural network (ANN), whereas [44] utilized a convolutional neural network (CNN) trained directly on raw time-series data. Both approaches demonstrated high classification accuracies—92% and 97%—under controlled conditions for defects such as wet discharge, surface discharge, sharp-point corona, and

internal discharge. However, performance declined significantly in string configurations. Specifically, at a distance of 3 meters, the accuracy dropped to 70.2%, which is a relatively short distance to observe substantial signal attenuation. This outcome highlights the limitations of manual feature extraction and raises concerns about the robustness of these methods in practical applications.

Manual feature extraction not only introduces biases from expert-dependent choices but also limits the model's ability to generalize effectively. Moreover, these studies were confined to controlled laboratory environments and addressed a limited range of defects, neglecting critical conditions such as punctured insulators.

Another significant limitation in the current literature is the assumption of a single defect per insulator, which rarely aligns with real-world conditions. In practice, defects often coexist, for instance, a broken disc may also exhibit DBA from contamination alongside hardware corona. Most existing models treat defects as mutually exclusive classes through single-label classification, overlooking complex and overlapping defect scenarios.

A study in [47] attempted to address this challenge by classifying combined contamination and perforation defects using ultrasonic signal features. However, simulating a puncture by drilling an open-ended hole poorly represents field conditions, as such a hole allows ultrasonic emissions to escape. In actual punctures, ultrasonic signals are encapsulated and attenuated by the porcelain and metal cap of the insulator. While most defect classes achieved accuracies ranging from 63.7% to 95.2%, the perforated insulator class performed poorly, with an accuracy of just 27%, significantly affecting the model's overall performance. Moreover, the study did not assess the model's generalizability across different insulator configurations, distances, or field conditions, limiting its practical relevance.

In real-world outdoor insulation systems, multiple defects often coexist amid various noise and interference sources, creating both a multi-class and multi-label classification problem. Although many studies have addressed single-label defect classification for outdoor insulators, more recent work has shifted toward multi-label classification for PD pattern recognition [48-49]. However, to date, this approach has not been extensively explored for outdoor insulator defect classification.

2.3 Thesis Objectives and Potential Contributions

This research proposes a non-intrusive method for assessing the condition of outdoor ceramic insulators via ultrasonic signatures. Unlike prior studies that relied on artificially induced defects in controlled laboratory settings, this work incorporates actual punctured samples obtained from field service, capturing more realistic conditions where ultrasonic signals are attenuated by porcelain and metal caps.

Ultrasonic data from various defect conditions will be collected to train and validate a deep learning model that employs a multi-label classification strategy, recognizing co-occurring defects such as DBA, punctures, and corona discharge. By leveraging convolutional neural networks (CNNs), the proposed framework eliminates the need for extensive manual feature engineering, enabling the automatic extraction of crucial features directly from the ultrasonic data.

To enhance the model's interpretability, Gradient-weighted Class Activation Mapping (Grad-CAM) is employed to pinpoint the critical temporal regions of ultrasonic signals that significantly influence the classification. This not only sheds light on each defect's unique ultrasonic characteristics but also provides a new avenue for defect characterization, addressing key limitations in existing work. Key objectives and contributions of this thesis include:

1. **Multi-Class Defect Classification:** Develop a robust ultrasonic-based approach for diagnosing outdoor ceramic insulators, including real punctured samples from field service.
2. **Model Validation and Testing:** Validate the proposed model under diverse insulator configurations, both in controlled laboratory conditions and in a real-world 138/13.8 kV substation.
3. **Multi-Label Defect Classification:** Create a framework capable of identifying overlapping defects (e.g., DBA, punctures, corona discharge) within a single insulator string.
4. **Temporal Feature Analysis:** Investigate and isolate the critical temporal features of ultrasonic signals that characterize each defect type, advancing our understanding of defect-specific ultrasonic behaviors.

Chapter 3

Materials and Methods

This chapter provides a comprehensive overview of the materials and methods used in this thesis, emphasizing the development and application of two distinct deep learning frameworks: a multi-class classification model and a multi-label classification model. It covers essential aspects, including the experimental methods used for data acquisition and the design and implementation of the deep learning models. Furthermore, this chapter outlines the procedures employed for testing and validation, ensuring the models' accuracy and robustness. Each step is described systematically to highlight the integration of experimental and computational approaches in achieving the research objectives.

3.1 Multi-Class Classification

3.1.1 Experimental Setup

The experimental setup utilized a 20kVA, 150 kV test transformer to generate the required high voltage. Acoustic signals were captured using a Sonaphone BS30 ultrasonic sensor, which operates within a frequency range of 20 kHz to 100 kHz and records data at a sampling rate of 256 kHz. The sensor was placed approximately two meters from the insulator string to ensure optimal signal detection. For each defect type, 60-second recordings were obtained to capture consistent and representative data.

The test objects consisted of two and three porcelain insulator discs arranged in a string formation. These insulators were deliberately subjected to various defects, including wet contamination, internal punctures, and corona discharge, to simulate real-world scenarios commonly encountered in high voltage systems.

A schematic representation of the experimental setup is presented in Figure 3.1, depicting the arrangement of the equipment and the positioning of the sensor relative to the test object. The Omicron MPD 600 PD monitoring system was incorporated into the

setup to ensure precise measurements and confirm the presence of a single type of discharge during testing. The system was connected to the test object using a coupling capacitor. The specifications of the Omicron MPD 600 are also provided in Table 2, further highlighting its capabilities in capturing reliable data. This configuration facilitated the acquisition of accurate signals, ensuring they accurately represented the defect under investigation.

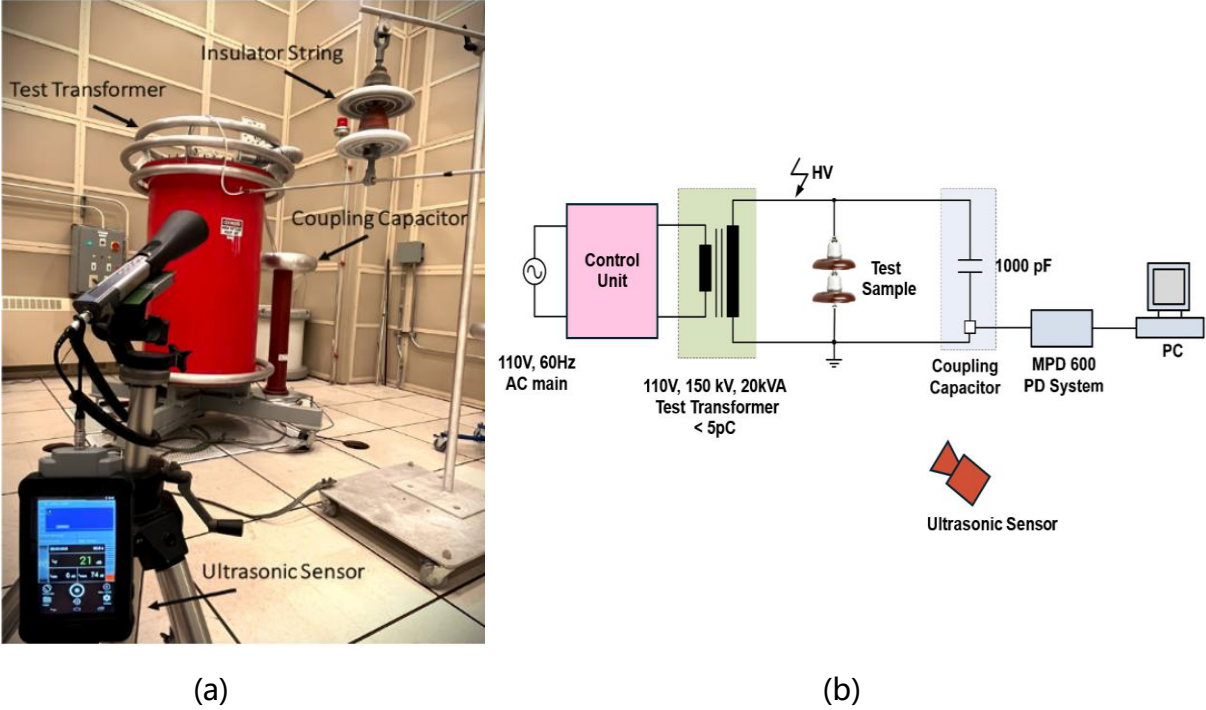


Figure 3.1 Acoustic measurement setup for detecting various insulator problems in an energized string. a) laboratory setup b) Schematic Diagram

Table 2 Omicron MPD 600 Specifications [50]

Center frequency	0 Hz - 32 MHz
Time domain	100 ns - 8 μ s
Input frequency range	V input: 0 Hz - 2.1 kHz PD input: 0 Hz - 20 MHz
Input impedance	V input: 1 M Ω (parallel 1 μ F) PD input: 50 Ω
Input voltage	V input: 60 V rms (max.) PD input: 10 V rms (max.)
Dynamic range	V input: 102 dB PD input: 132 dB (overall), 70 dB (per input)
Min. hardware	Pentium 4® / Athlon 64® or better, 1 GB RAM, USB 2.0
PD event time resolution	< 2 ns
System noise	< 0.015 pC
Spectrum analyzer noise	< -120 dB
Measurement accuracy	Voltage: \pm 0.05 % of calibrated V value Frequency: \pm 1 ppm PD level: \pm 2 % of calibrated PD value
Ambient temperature	Operation: 0 $^{\circ}$ C - 55 $^{\circ}$ C / 32 $^{\circ}$ F - 89 $^{\circ}$ F Storage: -10 $^{\circ}$ C - 70 $^{\circ}$ C / 14 $^{\circ}$ F - 158 $^{\circ}$ F
Power supply	8 V DC - 12,4 V DC

3.1.2 Data Collection Using Artificially Introduced Defects

In this study, three distinct defect types were artificially introduced under controlled laboratory conditions to replicate real-world scenarios. The following sections provide a detailed description of each defect type, including the methods of induction and their relevance to the data collection process.

To simulate typical in-service voltage stress, a voltage of 10 kV per disc was applied to each insulator string configuration. This choice aligns with practical field conditions, where, for instance, a 230 kV line (with a line-to-ground voltage of 132 kV) is typically distributed

across 14 discs, a 138 kV line (80 kV line-to-ground) across 8 discs, and a 69 kV line (40 kV line-to-ground) across 4 discs.

Applying a voltage of 10 kV per disc ensures that the experimental setup closely resembles actual operational scenarios, enabling reliable and meaningful data acquisition for defect analysis.

3.1.2.1 Corona Discharges

Corona discharges can be triggered by hardware-related issues or by the presence of a significantly non-uniform potential distribution along porcelain insulator strings.

These discharges typically occur under high voltage stress, particularly around areas such as the pin cement or between the base of the cap and the porcelain shell. Over time, continuous corona discharges may gradually erode the glaze layer on the porcelain shell, potentially weakening its mechanical strength and leading to "doughnut-type" failures, as discussed in prior studies [9]. However, such degradation is relatively uncommon due to the inherent durability of porcelain and the advancements in manufacturing techniques, which have significantly reduced the occurrence of such failures.

In the context of this study, corona discharges were primarily considered as a source of interference, particularly when their ultrasonic emissions overlap with those of other defects. This overlap can lead to challenges in accurately identifying and distinguishing between different defect types, which can affect the reliability of insulator condition assessments. Therefore, accurately differentiating corona discharges from other defects is essential for obtaining reliable data and ensuring the effectiveness of the diagnostic methods being employed.

To simulate corona discharges for this experiment, sharp-pointed end fittings were deliberately added to the insulators, as shown in Figure 3.2. These fittings created localized high electric field intensities, thus facilitating the generation of corona discharges. Two levels of corona discharge were introduced during the testing: a mild corona at 10 kV (inception voltage) and a severe corona at 20 kV (rated voltage of the string). The use of an image intensifier was essential to visually confirm the absence of surface discharges, ensuring that only corona ultrasonic signals were being recorded. This experimental setup

aimed to investigate the distinct characteristics of corona discharges and to quantify their influence on the overall data collected.

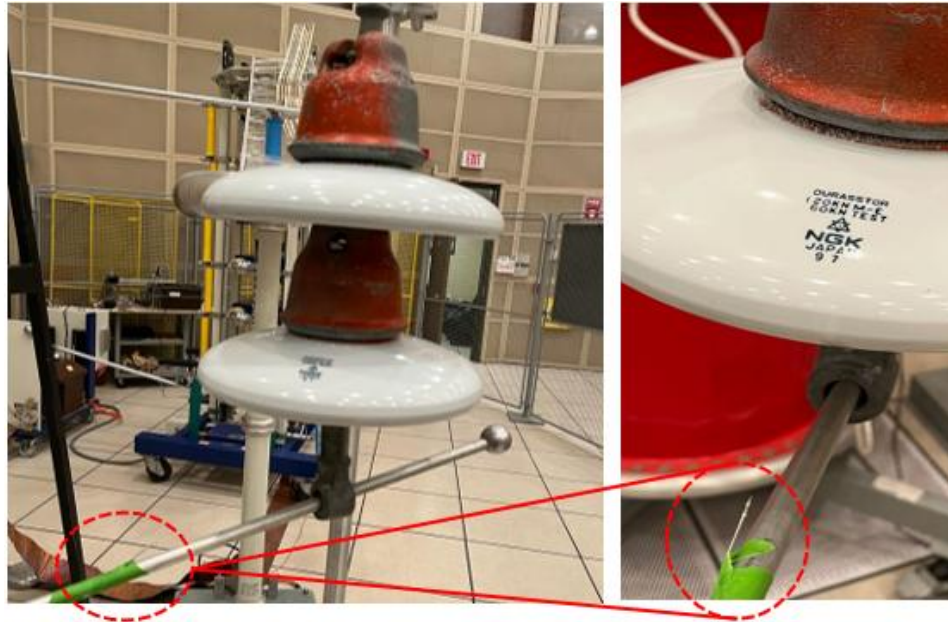


Figure 3.2 Hardware Corona generated by a sharp point attached near the HV end of the setup.

3.1.2.2 Dry Band Arcing (DBA)

To simulate DBA under controlled conditions, an insulator string was subjected to a systematic cleaning and contamination process. First, the insulator string was thoroughly washed using deionized water to remove any residual dirt or contaminants. It was then allowed to dry for 24 hours in a clean and controlled environment to ensure a dry and uniform surface. Following this, two contamination scenarios were simulated using solutions with distinct electrical conductivities, representing light and extreme contamination levels.

The light contamination level was achieved by applying a saline solution with an electrical conductivity of 1.43 S/m, resulting in an ESDD of 0.035 mg/cm². In contrast, the extreme contamination level was simulated using a more concentrated saline solution with an electrical conductivity of 11.2 S/m, corresponding to an ESDD of 0.28 mg/cm². These values align with the contamination classifications outlined in IEC 60507 standards [51], which

specify light contamination as having an ESDD in the range of 0.025 to 0.05 mg/cm² and extreme contamination as having an ESDD greater than 0.2 mg/cm².

Once the contamination process was completed, the insulator string was energized to a voltage of 20 kV to induce DBA. During these DBA events, ultrasonic signals were continuously monitored and recorded using the BS30 acoustic sensor. This voltage level was chosen to ensure reliable detection of ultrasonic emissions resulting from arcing activity. The ultrasonic data collected under both contamination conditions were subsequently analyzed to assess the characteristics and behavior of DBA in relation to contamination severity.

3.1.2.3 Punctured Insulators

Punctured insulators, sourced from a local utility company, were subjected to comprehensive validation tests to assess their condition. Initially, the insulators appeared to be in good physical condition; however, insulation resistance and tan delta measurements were performed to evaluate their electrical properties. These tests revealed a significant compromise in insulation quality when compared to a set of known healthy insulators, as summarized in Table 3. This discrepancy indicated that, despite their seemingly intact exterior, the punctured insulators had deteriorated electrically, potentially affecting their performance in high voltage applications.

To further investigate the impact of this damage, the punctured insulators were incorporated into two-disc insulator strings. These strings were configured in two different arrangements: alternating the positions of the damaged and healthy discs to simulate real-world operating conditions where defective insulators might exist within a string of operational insulators. The insulator strings were then subjected to a high voltage stress of 20 kV to replicate operational conditions that could induce potential failures or malfunctions. Subsequently, ultrasonic signals were captured for each string configuration, enabling a comparison of the acoustic emissions from strings with varying combinations of damaged and healthy insulators. This approach was designed to investigate how punctured insulators influence the overall acoustic signature of the string and to assess whether the ultrasonic data could be used to reliably distinguish between damaged and

healthy insulators within a string configuration. The collected data serves as a critical component for developing diagnostic models aimed at identifying and quantifying damage in high voltage insulator systems.

Table 3. Health Condition of the Punctured vs healthy insulators

Insulator	Insulation Resistance	Tan-Delta
Healthy #1	24.9 G Ω	4.1%
Healthy #2	10 G Ω	5.3%
Punctured	11.83 M Ω	258.2%

3.1.3 Data Preprocessing

The captured 60-second ultrasonic signals from various defects were segmented into smaller frames of 10 milliseconds. This segmentation approach was adopted to preserve critical pulse information essential for defect classification while simultaneously improving the computational efficiency of the model. Subsequently, the segmented ultrasonic waveforms were subjected to Z-score normalization as described in the equation below:

$$Z = \frac{X - \mu}{\sigma} \quad (1)$$

Where Z being the normalized value (Z-score), X represents the signal's amplitude, μ is the mean of the dataset and σ is the standard deviation of the dataset. This preprocessing technique standardizes signal amplitudes, thereby improving classification accuracy and enhancing the model's generalizability across varying signal intensities.

3.1.4 Multi-Class 1D-Convolutional Neural Network Model

CNNs have become a prominent architecture in the field of deep learning, renowned for their ability to produce robust and high-performance models. A significant advantage of CNNs is their capacity to autonomously learn a hierarchy of features from input data, enabling efficient and accurate classification. Originally developed for image processing

applications, their scope has expanded to encompass the analysis of one-dimensional data, including time-series signals and ultrasonic waveforms [52–53].

The architecture of a conventional CNN consists of three primary layers: convolutional, pooling, and fully connected layers, each contributing uniquely to the model's learning process. In our network architecture, four trainable layers are employed: three convolutional layers followed by a fully connected layer. The convolutional layers act as feature extractors, utilizing learnable filters to perform convolution operations across the input data and capturing local patterns and features. The convolutional operation for each filter can be expressed as:

$$y_i^{(k)} = \sigma \left(\sum_{j=1}^M x_{i+j-1} * w_j^{(k)} + b^{(k)} \right) \quad (2)$$

Where:

- x_{i+j-i} is the input at position $i+j-1$
- $w_j^{(k)}$ is the weight of the k -th filter (kernel) at position j .
- $b^{(k)}$ is the bias of the k -th filter.
- σ is the activation function (e.g., ReLU, $\sigma(z) = \max(0, z)$).
- M is the kernel size.
- $y_i^{(k)}$ is the feature map value at position i for the k -th filter (or kernel) after applying the convolution operation

For K filters, this equation is applied K times to produce K feature maps. To enable the network to model complex non-linear relationships, rectified linear unit (ReLU) activation functions are applied after each convolutional layer.

Subsequent max pooling layers are incorporated to reduce the dimensionality of the feature maps, allowing the network to detect features across broader regions of the input data. The max pooling operation is mathematically expressed as:

$$y_i = \max(x_i, x_{i+1}, \dots, x_{i+p-1}) \quad (3)$$

Where P is the pooling window size. This operation reduces the dimensionality by selecting the maximum value within each window of size P.

To minimize overfitting and improve generalization, a dropout layer is introduced, randomly deactivating 50% of the neurons during training. This strategic layer configuration enhances the network's ability to learn robust representations while maintaining computational efficiency. The output of the dropout layer is given by:

$$y_i = \begin{cases} 0 & \text{with probability } p \\ \frac{x_i}{1-p} & \text{with probability } 1 - p \end{cases} \quad (4)$$

Where p represents the dropout rate, which is the probability of deactivating a neuron during training. In this case, P = 0.5, meaning 50% of the neurons are randomly set to zero during each training iteration. This process helps prevent overfitting by forcing the network to learn more robust and generalized features, as it cannot rely on any single neuron consistently.

The network concludes with fully connected layers, which integrate the extracted features to perform classification. The final layer outputs the probability distribution across the classes using a SoftMax activation function, which is defined as:

$$y_C = \frac{e^{z_C}}{\sum_{k=1}^C e^{z_k}} \quad (5)$$

Where Z_C is the raw score for class c, Z_k is the raw score of all classes $k=1,2,3,\dots,C$. and C is the total number of classes. If the layers are combined in a sequence such as convolution, ReLU, max pooling, dropout, fully connected and SoftMax, the overall transformations can be described by chaining these equations step by step, as illustrated in Figure 3.3, which depicts our model architecture. The model, designed for multi-class classification, was trained by minimizing the categorical cross-entropy loss function, described in equation (6), leveraging the Adam optimizer [54] for efficient and adaptive learning. The implementation was conducted using the Keras and TensorFlow libraries within the Python programming environment.

$$\mathcal{L} = -\frac{1}{N} \sum_{i=1}^N \sum_{c=1}^C y_{i,c} \log(\hat{y}_{i,c}) \quad (6)$$

where:

N: Total number of samples in the batch.

C: Total number of classes.

$y_{i,c}$: True label for sample i , where $y_{i,c} = 1$ if sample i belongs to class c , and 0 otherwise.

$\hat{y}_{i,c}$: Predicted probability for class c for sample i (output of the SoftMax function).

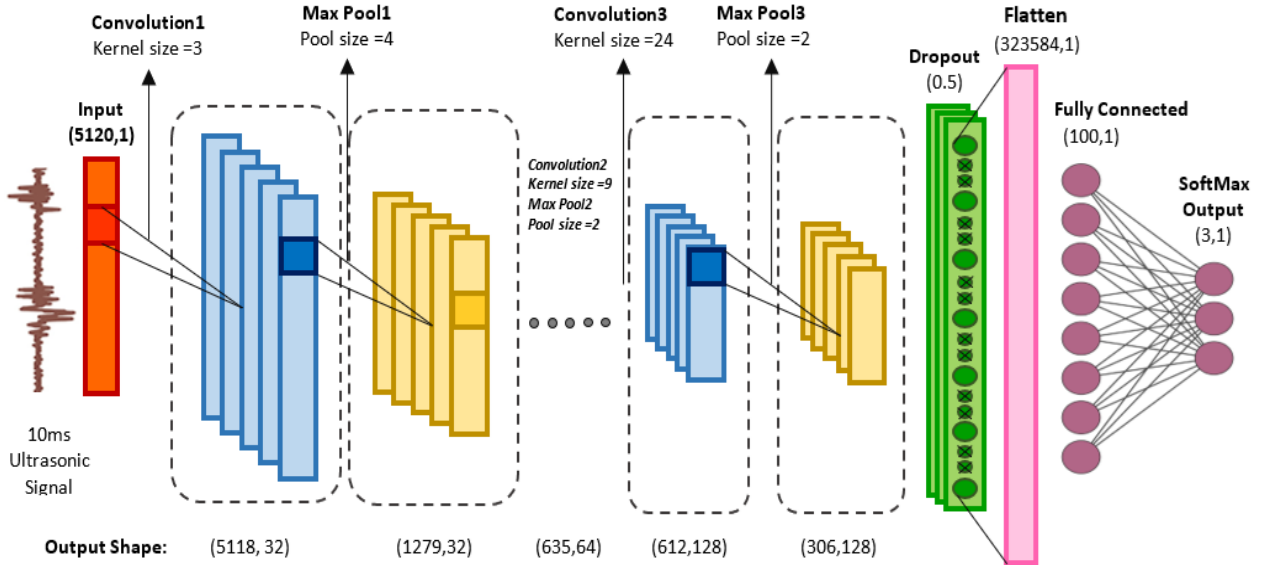


Figure 3.3 Proposed 1D-CNN Architecture

3.1.5 Multi-Class Performance Metrics

In multi-Class problems, the model's performance is assessed using accuracy, precision, recall and F1 score metrics, which provides a comprehensive evaluation of its effectiveness in classifying various defect types. These metrics not only highlight the model's strengths but also identify areas for potential improvement. Precision, as defined in Eq. (7), represents the percentage of correctly identified positive instances out of all predicted positives, where TP is the number of true positives and FP is the number of false positives.

$$\text{Precision} = \frac{\text{TP}}{\text{TP} + \text{FP}} \quad (7)$$

Recall, outlined in Eq. (8), evaluates the proportion of actual positive instances correctly identified by the model, where FN is the number of false negatives.

$$\text{Recall} = \frac{\text{TP}}{\text{TP} + \text{FN}} \quad (8)$$

The F1 score, described in Eq. (9), combines precision and recall into a single metric, offering a balanced measure that considers both false positives and false negatives:

$$\text{F1} = 2 \times \frac{\text{Precision} \times \text{Recall}}{\text{Precision} + \text{Recall}} \quad (9)$$

Finally, accuracy is defined as the ratio of correctly classified instances to the total number of instances, as defined in Eq. (10), Where TN is the number of true negatives.

$$\text{Accuracy} = \frac{\text{TP} + \text{TN}}{\text{TP} + \text{TN} + \text{FP} + \text{FN}} \quad (10)$$

While accuracy provides an overall performance metric, it can be misleading in cases of class imbalance. For instance, in datasets with a dominant class, a model that consistently predicts the majority class may attain high accuracy but fail to accurately classify the minority class.

To overcome this limitation, precision and recall are utilized, offering a more nuanced understanding of the model's performance, particularly in identifying positive instances and addressing class imbalances. Precision measures the quality of positive predictions, while recall ensures the model captures most actual positives. The F1 score further combines these aspects, providing a more comprehensive evaluation than accuracy alone.

Additionally, confusion matrices are used to visualize classification results and uncover misclassification patterns. The insights derived from these analyses can guide the optimization of the model, leading to enhanced performance in subsequent iterations.

3.1.6 CNN Interpretability using Grad-CAM

CNNs have demonstrated exceptional performance in various classification tasks, including the detection of insulator defects using ultrasonic signals. However, their inherent lack of transparency poses challenges in understanding how these models arrive at their predictions.

Grad-CAM [55] is a robust technique designed to enhance the interpretability of CNNs by visualizing the specific features within the input data that contribute most significantly to the model's predictions. This method is particularly valuable for understanding the decision-making process of CNNs. By applying Grad-CAM to our trained CNN, we can generate heatmaps that highlight the regions of the ultrasonic signal most influential in the model's classification decisions.

The process of generating a Grad-CAM heatmap begins by computing the gradient of the class score with respect to the feature maps in the final convolutional layer. The gradient, denoted as:

$$\text{Grad} = \frac{\partial y^c}{\partial A^k} \quad (11)$$

measures the contribution of each feature map, A^k , to the predicted class score y^c . Here, k represents the number of feature maps, which is 128 in our model. These gradients provide insight into how the individual feature maps influence the final prediction. To determine the overall importance of the k -th feature map for the c -th class output, the gradients are spatially averaged across all elements of the feature map as follows:

$$\alpha_k^c = \frac{1}{Z} \sum_{i=1}^Z \frac{\partial y^c}{\partial A_i^k} \quad (12)$$

In this equation, Z represents the length of one feature map ($Z=612$ in our case), and A_i^k is the i -th element of the k -th feature map. The resulting average gradients, α_k^c , act as weights indicating the relative importance of each feature map for the predicted class. Using these weights, a weighted combination of the feature maps is calculated to generate the Grad-CAM heatmap. To focus exclusively on the features that positively influence the

prediction, a ReLU operation is applied, setting all negative values to zero. This process is mathematically expressed as:

$$L_{\text{Grad-CAM}}^c = \text{ReLU}(\sum_k \alpha_k^c A^k) \quad (13)$$

Since the feature maps in the final convolutional layer are typically smaller than the input dimensions, the resulting heatmaps are upscaled to match the input size. This upscaling ensures that the heatmap provides a clear and detailed visual representation of the regions within the input data that the model focused on during its decision-making process.

Grad-CAM thus offers valuable insights into the inner workings of convolutional neural networks, helping to enhance the interpretability of model predictions and build trust in their reliability for tasks such as classifying ultrasonic signals associated with insulator defects.

3.1.7 Laboratory Testing

The model's performance was assessed through a two-stage testing process conducted within a controlled laboratory environment. In the first stage, the dataset, consisting of segmented 10-millisecond ultrasonic signals, was divided into an 80% training set and a 20% testing set. This division resulted in a total of 18,000 signals, with 3,600 allocated for testing.

In the second stage, new data were introduced to evaluate the model under varied conditions, including a three-disc string configuration energized at 30 kV. Corona discharges were induced using a sharp point affixed to the high-voltage side, DBA was initiated with a solution of 7.5 mS conductivity, and a punctured disc was positioned at the center of the three-disc string. Ultrasonic signals, each 30 seconds in duration, were collected from all three defect types for testing. This phase was designed to challenge the model with scenarios not encountered during initial training, providing an assessment of its adaptability and robustness. The decision-making window size was maintained at 10 milliseconds, resulting in a second testing set comprising 9,000 signals. This approach ensured a comprehensive evaluation of the model's performance across a broader spectrum of defect manifestations.

3.1.8 Field Testing

The trained model demonstrated its ability beyond the laboratory environment by being deployed in a 138/13.8 kV substation to identify potential defects in a real-world setting. Elevated ultrasonic emissions were identified in specific substation components, notably the load break switches (LBS) and cap-pin ceramic insulators located on the left-hand side, as illustrated in Figure 3.4. Subsequent drone inspections revealed the presence of ice on the surfaces of these components. The melting process of the ice induced DBA, which was systematically monitored and analyzed using ultrasonic sensing.

Figure 3.5. presents ultrasonic measurements recorded during and after the ice melting process on the insulator and LBS surfaces. After 2–3 hours, most ultrasonic emissions ceased, indicating the termination of DBA following the complete melting of the ice. Measurements were conducted at distances of approximately 15 m from the sensor to the LBS and 25 m to the insulator. The temporal reduction in ultrasonic emissions, closely correlated with the melting ice, further validates the model's capability to detect and distinguish between transient and persistent defects.

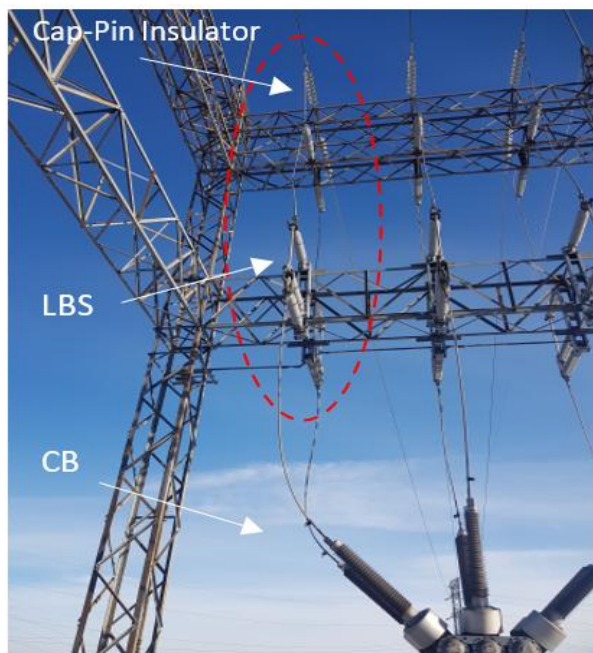
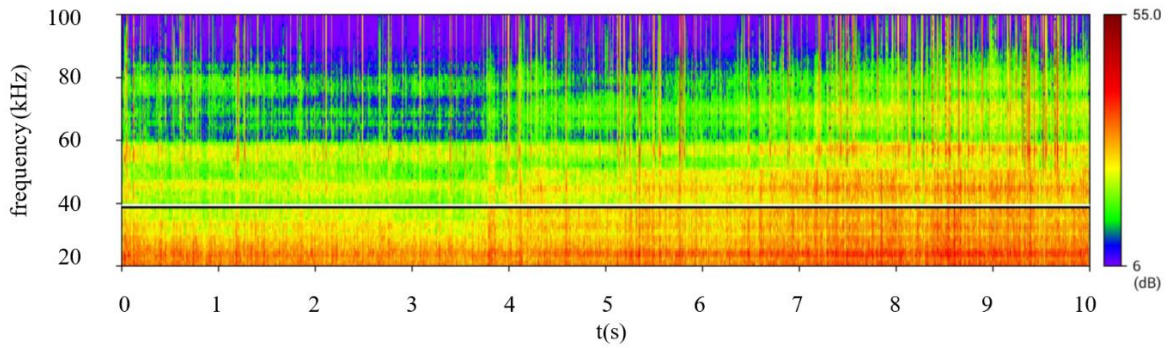
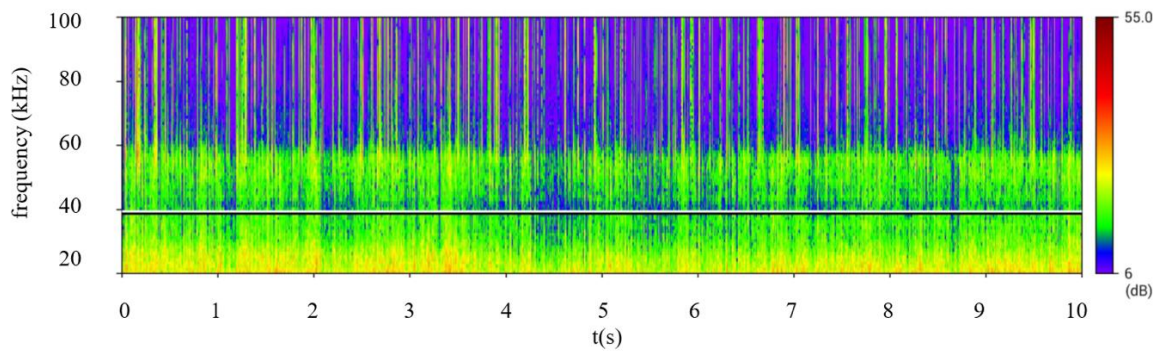


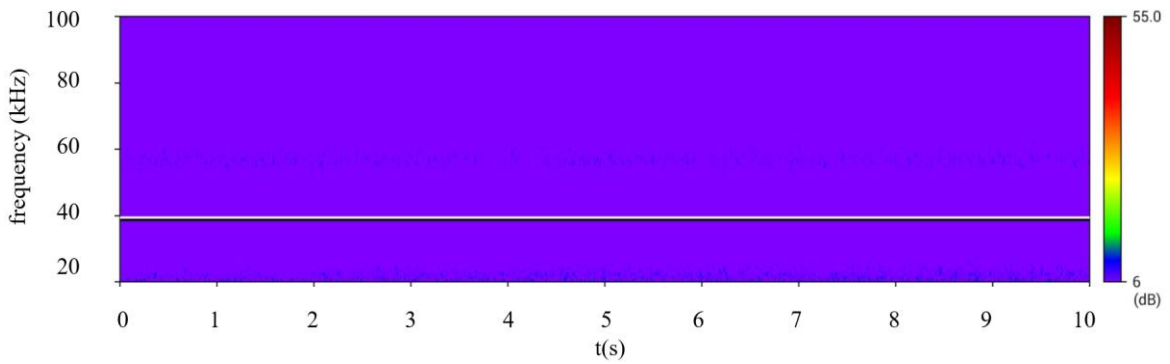
Figure 3.4 DBA observed on the ceramic insulator and LBS, highlighted by a red circle is a consequence of ice melting process.



(a)



(b)



(c)

Figure 3.5 Ultrasonic measurements at different stages:

- a) During ice melting on LBS
- b) During ice melting on cap-pin insulator
- c) After the complete melting of ice on both components

After the complete melting of ice from various substation components, a comprehensive ultrasonic scan was conducted. The sensor detected mild ultrasonic activities on the middle phase of the lightning surge arrester for the 138/13.8 kV transformer, as shown in Figure 3.6 and 3.7. Subsequent investigation confirmed a loose connection in the arrester, which was identified as the source of corona discharges.

This finding underscores the technique's potential for advanced substation diagnostics, offering a non-intrusive and effective approach to identifying and visualizing defects that could compromise the reliability and efficiency of power transmission systems.



Figure 3.6 Loose connection on transformer surge arrester highlighted in red circle.

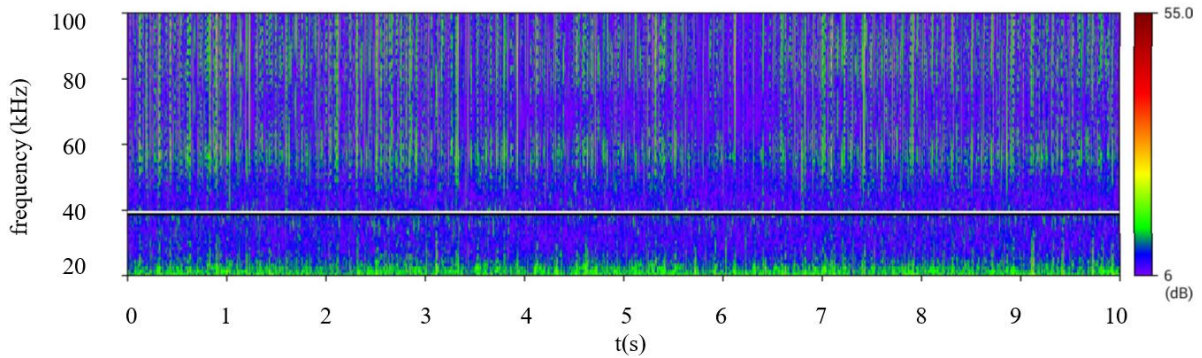


Figure 3.7 Ultrasonic measurement capturing Corona discharges arising from loose connection at transformer surge arrester

3.2 Multi-label Classification

3.2.1 Experimental Setup

In this experiment, a 200 kVA, 400 kV test transformer was utilized to generate the high voltage required for testing porcelain insulators arranged in strings of two and three discs. The insulators were subjected to various defects, including wet contamination, internal punctures, and corona discharge, along with combinations of these defects. This resulted in a total of six distinct classes: three individual defects, their combinations, and a healthy (defect-free) class. The objective was to capture acoustic signatures corresponding to both individual defects and the interactions arising from multiple concurrent defects. These interactions often generate overlapping ultrasonic signals, which are crucial for developing precise diagnostic models. To facilitate this process, acoustic emissions were captured under controlled laboratory conditions using an ultrasonic sensor (Sonaphone BS30) placed 2 meters away, as described in section 3.1.1. The experimental setup is illustrated in Figure 3.8.

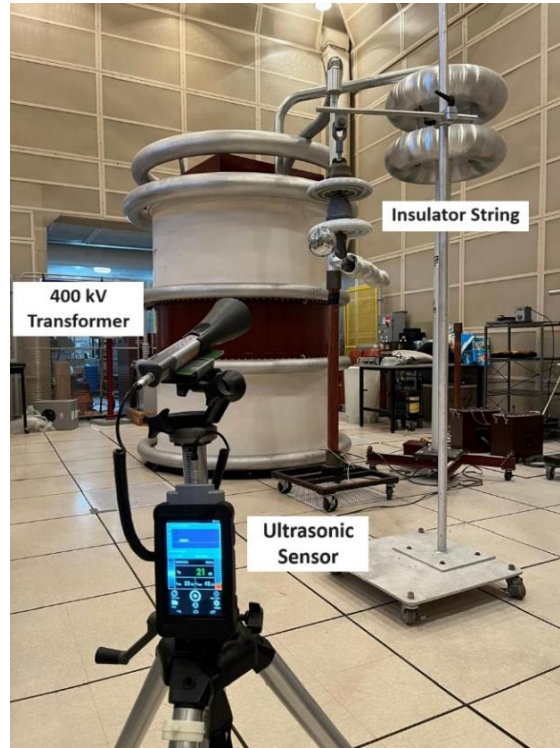


Figure 3.8 Laboratory experimental setup

3.2.2 Data Collection using Multiple concurrent defects

Four distinct datasets were collected to support model development and evaluation. Two datasets were combined for training and fine-tuning the model, while the remaining two were reserved exclusively for testing. This approach ensured the model was exposed to a broad range of conditions, enhancing its robustness and generalization capabilities. The classification framework encompassed four main classes: healthy, DBA, puncture, and corona discharge. To account for defect interactions, two additional concurrent classes (DBA+Corona and Puncture+Corona) were introduced, resulting in a total of six classes. These six classes represent all physically feasible combinations of the defects observed in the field.

Certain other combinations, such as DBA and surface discharges induced by punctured insulators [56], were excluded as they are not physically feasible. This limitation arises due to the change in the electric field distribution caused by the defects. Specifically, when an

insulator becomes wet and contaminated, the electric field transitions from capacitive grading, which supports PD activity, to resistive grading, where the surface conductivity dominates. This shift effectively suppresses any PD activity, as the current flow becomes resistive and no longer supports the localized ionization processes required for discharges. Therefore, combinations involving defects that disrupt or negate discharge mechanisms, such as wet contamination with puncture-induced surface discharges, were excluded from the classification framework.

Building on these considerations, defective conditions were carefully simulated to create realistic datasets for classification. Insulators were energized at a voltage of 10 kV per disc, resulting in total voltages of 20 kV for two-disc configuration and 30 kV for three-disc configuration. To replicate varying severities of corona discharges, three distinct sharp-point profiles were affixed to the insulator end fittings. For simulating DBA, healthy insulator strings were thoroughly cleaned, dried, and sprayed with solutions of varying electrical conductivities (1.4 S/m, 4 S/m, and 11.2 S/m), to represent equivalent ESDD levels of light (0.035 mg/cm^2), moderate (0.1 mg/cm^2), and heavy (0.28 mg/cm^2) contamination respectively, as specified by the IEC 60507 standards [51].

For the punctured class, two defective insulators removed from service were examined. The insulator strings were configured in four distinct arrangements, alternating the positions of the punctured and healthy discs. In some configurations, the punctured discs were placed closer to the high-voltage side, while in others, they were positioned nearer to the grounded side.

The first three datasets were collected using a two-disc configuration, while the fourth dataset utilized a three-disc setup. Each dataset comprised 9,000 ultrasonic signals, with each signal lasting 40 milliseconds. This duration was chosen to ensure the capture of at least two discharge pulses from the defect type exhibiting the lowest frequency. Similar to the multi-class problem, the ultrasonic waveforms underwent preprocessing with Z-score normalization. Table 4 provides details of the disc conditions based on tan delta and insulation resistance measurements, while Table 5 summarizes the dataset conditions derived from these configurations.

Table 4. Disc Conditions based on Tan and Insulation Resistance Measurement

Disc No.	Tan δ (%)	Insulation Resistance (Ohm)
1	2.9	90.1 G Ω
2	3.3	35 G Ω
3	4.4	24.6 G Ω
4	127.6	19.2 M Ω
5	235	12.4 M Ω

Table 5. Summary of Datasets

Class Type	Two-Disc Configuration (20 kV)		Three-Disc Configuration (30kV)	
	Training/Validation/Testing (70% / 10% / 20%)		Testing #1	Testing #2
	Dataset #1	Dataset #2	Dataset #3	Dataset #4
Healthy	Disc1 Disc2	Disc2 Disc3	Disc1 Disc3	Disc 1 Disc2 Disc3
DBA Conductivity (S/m)	1.5	6	3	6
Punctured	Disc1 Disc4	Disc4 Disc2	Disc3 Disc5	Disc1 Disc2 Disc5
Corona	Fine Sharp point 0.5mm tip thickness	Blunt Sharp point 3 mm tip thickness	Hollow Sharp pipe 2 mm wall thickness, 20mm diameter	Fine Sharp point 0.5mm tip thickness

3.2.3 1-D Convolutional Neural Network for Overlapping Defects

This model accommodates overlapping defects by enabling the assignment of multiple labels to a single data point, thereby framing the classification task as both multiclass and multilabel.

In the multiclass approach, these overlapping defects are treated as unique combinations, forming entirely new and distinct classes. For example, simultaneous occurrences of corona discharge and DBA are categorized as a separate class, distinct from individual defects. While this method simplifies the output by assigning a single label to each data point, it significantly increases the number of classes. All potential combinations must be predefined, resulting in exponential growth as the number of defects classes increases. This not only raises computational costs but also poses substantial challenges in training the model effectively.

The multilabel approach, by contrast, assumes that each base defect outputs an independent probability. This allows the identification of multiple co-occurring defects without merging them into a single combined class. As a result, it offers greater flexibility and scalability, especially in scenarios where defect combinations are not exhaustive or predefined.

However, since this study considers only two defect combinations, the multiclass approach is more practical and appropriate. The multilabel approach, as noted earlier, could introduce physically invalid combinations, making it less suitable for this particular case. The proposed CNN model accommodates possible defect combinations by defining six distinct classes: healthy, punctured, DBA, corona, punctured with corona, and DBA with corona. The architecture of the CNN model is depicted in Figure 3.9.

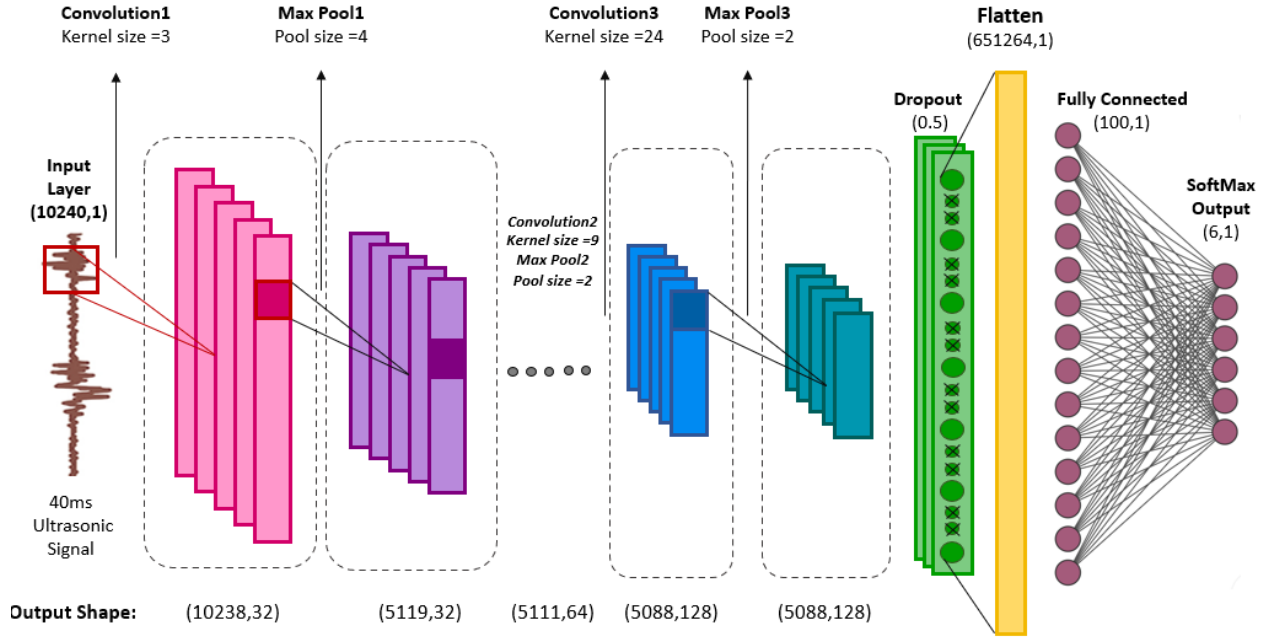


Figure 3.9 Proposed 1D-CNN Architecture for overlapping defects

3.2.4 Multi-Label Classification Performance Metrics

In multi-label classification problems, accuracy can be an overly strict metric, as it only considers predictions correct when all labels are perfectly matched. This overlooks cases where some, but not all, labels are accurately predicted. To offer a more balanced evaluation, the Hamming score is used. The Hamming score measures the average fraction of correctly predicted labels across all instances, making it a more suitable metric for multi-label classification. The formula for the Hamming score is provided in Eq. (14).

$$\text{Hamming score} = \frac{1}{N} \sum_{i=1}^N \frac{|y_i \cap \hat{y}_i|}{|y_i \cup \hat{y}_i|} \quad (14),$$

where N represents the total number of instances, y_i is the set of true labels for instance i , and \hat{y}_i is the set of predicted labels for instance i . The intersection $|y_i \cap \hat{y}_i|$ indicates the number of correctly predicted labels, while the union $|y_i \cup \hat{y}_i|$ represents the total number of true and predicted labels for that instance. This approach provides a more balanced evaluation by accounting for partial correctness in multi-label scenarios.

Chapter 4

Results and Discussion

4.1 Punctured Disc Detection

The results of this study begin with an observation from preliminary experiments. When a punctured insulator was integrated into a string of healthy insulators, distinct behavioral patterns were noted. Using the experimental setup described in Section 3.1.1, various configurations of insulator discs were tested, revealing key phenomena that set the stage for the classification results presented later in this chapter. Table 3 summarizes the insulator conditions examined in this investigation.

4.1.1 Configuration 1: A string of two healthy discs

In this configuration, two healthy ceramic insulator discs (1 and 2) were arranged in a string and subjected to a voltage of 30 kV. The classical PD detector did not identify any signs of partial discharge activity on the insulators. However, minimal background noise, measured in picocoulombs, was detected, as shown in Figure 4.1. Furthermore, observations using the image intensifier and acoustic measurements confirmed the absence of surface discharge activity on the insulators, as illustrated in Figure 4.2. This scenario serves as a baseline for comparison with subsequent configurations.

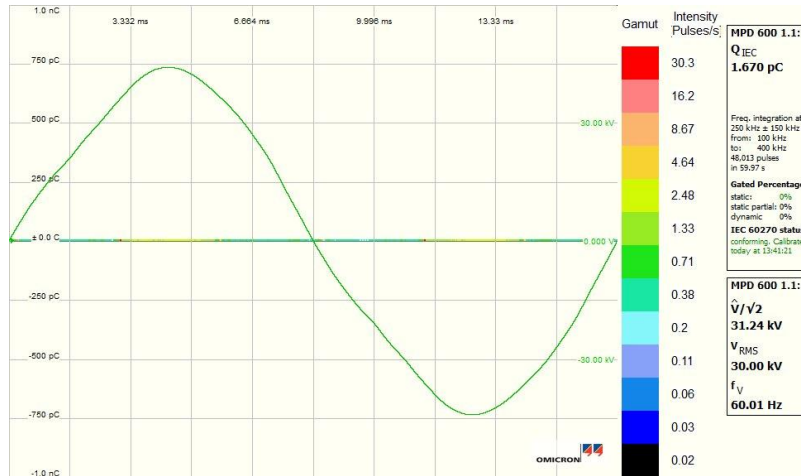


Figure 4.1 1~2 pC of noise observed on the classical PD detector.

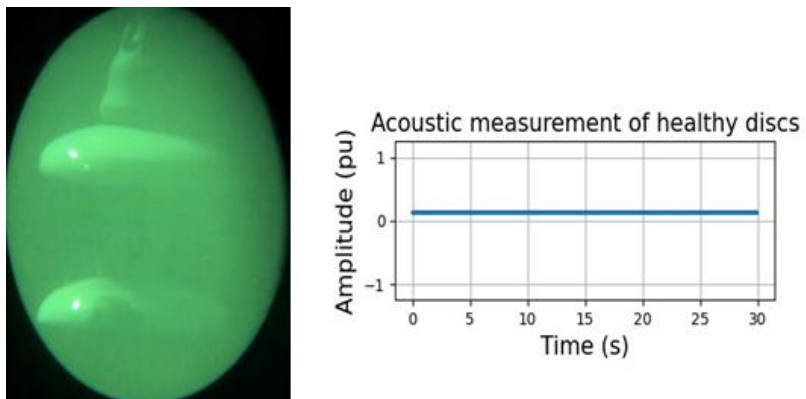


Figure 4.2 Image intensifier and acoustic measurements show no signs of surface discharge activities.

4.1.2 Configuration 2: A string of defective disc near the high voltage end

In the second configuration, the healthy disc (#1) was placed near the ground end, while the defective disc was positioned near the high voltage side. PD activities within the range of hundred pico-coulombs were observed using a classical PD detector as shown in Figure 4.3. Scanning the ceramic insulator string with an ultrasonic sensor revealed that most ultrasonic emissions originated from the healthy disc, particularly at the triple junction

where the metallic cap, porcelain shell, and air meet. This observation was further confirmed using an image intensifier, as illustrated in Figure 4.4.

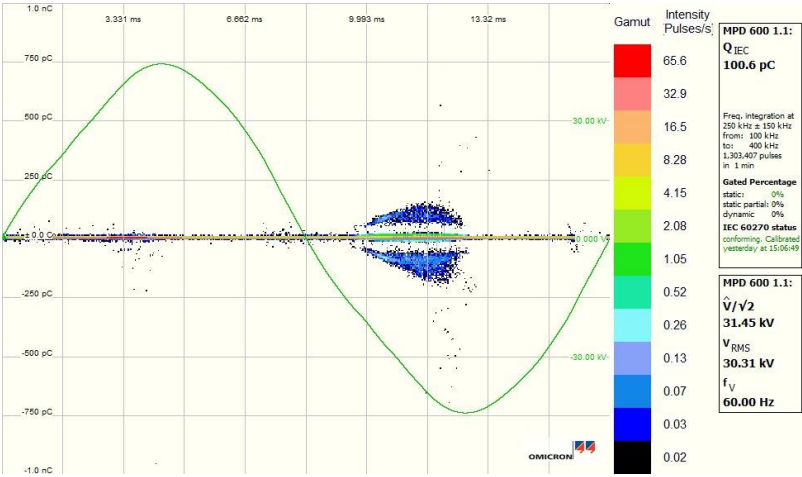


Figure 4.3 100 pC of surface discharges observed on the classical PD detector

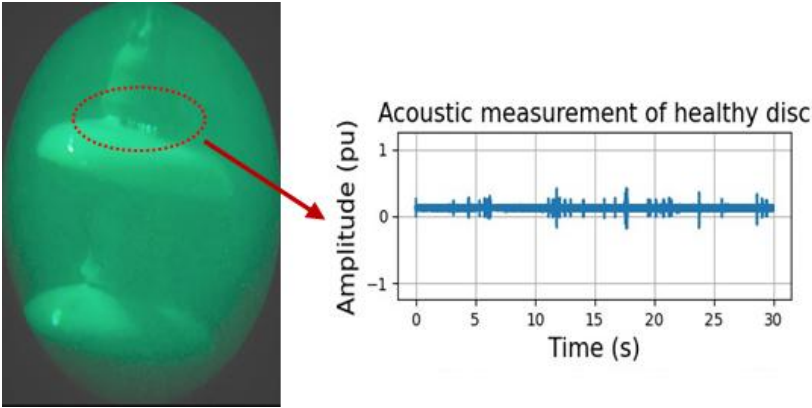


Figure 4.4 Surface discharges predominantly emanating from the healthy disc, as depicted in the image intensifier and acoustic measurement of the insulator string.

4.1.3 Configuration 3: A string of defective disc near the ground end

In the third configuration, the healthy insulator (#1) was positioned near the high-voltage side, while the defective insulator was located near the ground end. Although weaker PD activities were measured (approximately 50 pC), as shown in Figure 4.5, a consistent pattern emerged. Surface discharges persisted on the healthy insulator, as confirmed by acoustic measurements and image intensifier images, as illustrated in Figure 4.6.

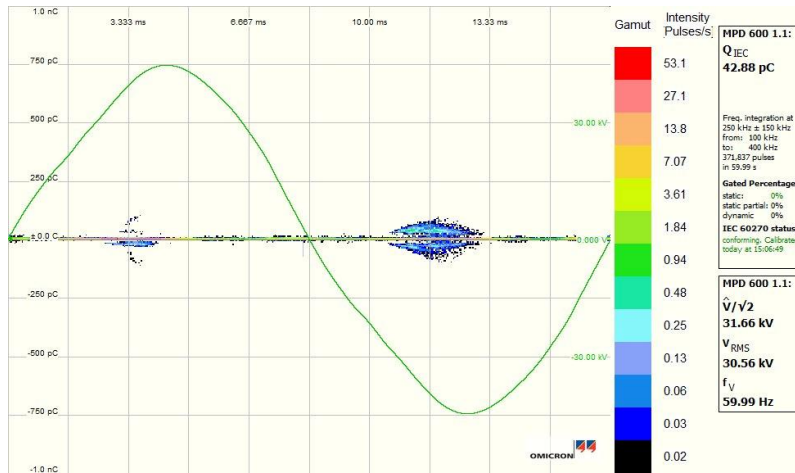


Figure 4.5 Approximately 50 pC of surface discharges were observed on the classical PD detector.

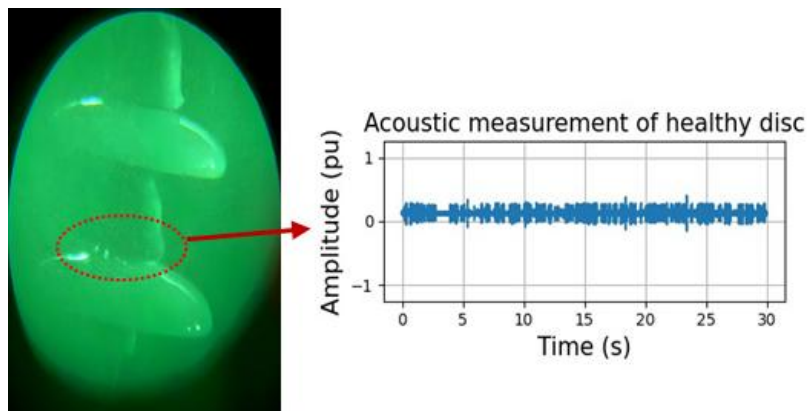


Figure 4.6 Surface discharges persisted on the healthy insulator, as depicted in the image intensifier and acoustic measurement of the insulator string.

4.1.4 A string of three discs

To further validate the observations, the experiment was conducted using all three discs listed in Table 3. The defective disc was positioned at the bottom of the string, near the high-voltage end, while the healthy discs were placed in the middle and at the top of the string, near the ground end. A voltage of 45 kV was applied to the string using a test transformer. Intense surface discharges, measuring 255 pC, were observed on both healthy discs, with no discharges detected on the defective insulator. PD activities and ultrasonic emissions originating from the triple-point interface of the healthy discs were detected through image intensifier and acoustic scans, as illustrated in Fig. 4.7 and 4.8, respectively.

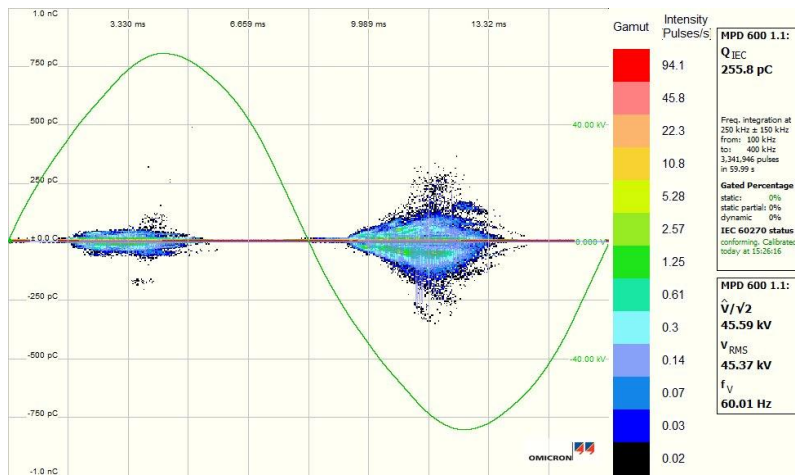


Figure 4.7 Approximately 255 pC of surface discharges were observed on the classical PD detector.

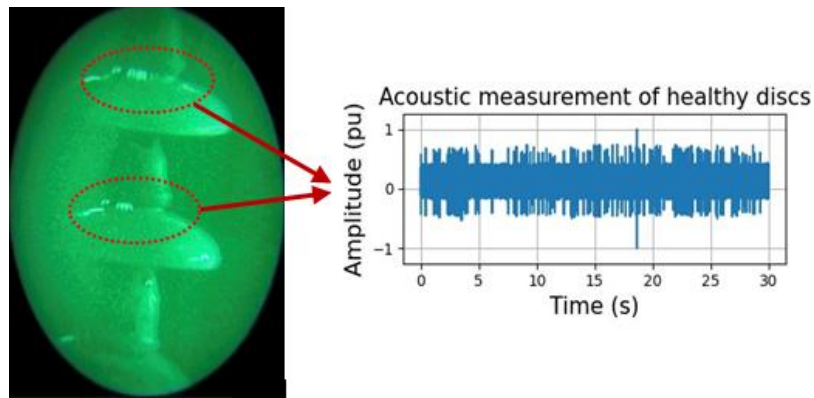


Figure 4.8 Surface discharges emanating from the healthy insulators, as depicted in the image intensifier and acoustic measurement of the insulator string.

The findings demonstrate that when all discs in an insulator string are healthy, the electric stress is uniformly distributed, effectively preventing surface discharges. However, if one or more discs are punctured, they fail to withstand the applied stress, forcing the remaining healthy discs to bear a disproportionate stress load. This redistribution of stress significantly increases the likelihood of surface discharges on the unaffected discs. In essence, punctured insulators can adversely affect adjacent healthy insulators by inducing surface discharges on them. This effect becomes more pronounced when the string is shorter, or the number of punctured discs increases.

These phenomena were effectively captured by the ultrasonic sensor due to its directional characteristics. Consistent outcomes were achieved across various experimental configurations, demonstrating the reliability of the method. While image intensifiers and corona cameras are also capable of detecting surface discharges, they face significant challenges in distinguishing whether these discharges are caused by cracks, contamination, or punctured discs. In contrast, ultrasonic signals, particularly when analyzed using well-trained machine learning or deep learning models, provide a robust and reliable means of differentiation, as supported by previous research [57-59].

4.2 Multi-Class Classification Results

4.2.1 Laboratory Testing Results

The confusion matrices generated from the laboratory testing conducted in stages 1 and 2 (Highlighted in Figures 4.9 and 4.10) demonstrate remarkable model accuracies of 99.64% and 96.71%, respectively. The slight decrease in accuracy in stage 2 can be attributed to the inclusion of diverse insulator configurations and operating conditions, which tested the model's adaptability. These results highlight the model's robustness while also indicating potential areas of improvement.

A noteworthy observation is the model's slight confusion in distinguishing between hardware corona and triple-point discharge. This confusion is likely due to the similarities in their acoustic patterns and discharge characteristics, suggesting a need for improved

feature extraction techniques or additional training data to enhance classification accuracy for closely related defect types.

Despite these challenges, the model demonstrated exceptional performance in detecting DBA, characterized by its distinct acoustic signatures. This achievement underscores the model's effectiveness in identifying critical insulator defects. Given that DBA often serves as an early indicator of more severe failures, this capability is especially valuable for maintaining the reliability and safety of high-voltage systems.

Actual Values	DBA	1200	0	0
	Corona	0	1200	0
	Triple	0	13	1187
		DBA	Corona	Triple
		Predicted Values		

Figure 4.9 Confusion matrix for laboratory testing (Stage 1)
(Overall Classification Accuracy: 99.64%)

Actual Values	DBA	2935	65	0
	Corona	0	2906	94
	Triple	0	137	2863
		DBA	Corona	Triple
		Predicted Values		

Figure 4.10 Confusion matrix for laboratory testing (Stage 2)
(Overall Classification Accuracy: 96.71%)

4.2.2 Field Testing Results

4.2.2.1 Model Evaluation Metrics

Field testing further validated the model's effectiveness, demonstrating high accuracy in detecting hardware corona and DBA. However, some discrepancies were observed, particularly in DBA detection at greater distances (Table 6). Notably, hardware corona detection achieved a classification accuracy of 98.8%, while DBA occurrences on the LBS positioned approximately 15 meters away, were identified with 100% accuracy.

The primary source of errors stemmed from DBA instances on cap-pin insulators located about 25 meters away, where classification accuracy dropped to 75.4% due to signal attenuation. These weakened signals reduced the model's overall classification accuracy to 91.4%. This decline underscores the challenges posed by distance-related signal attenuation.

Despite these limitations, the model demonstrated a high degree of confidence in predicting DBA events, particularly when cumulative decision-making was applied over a 10-second window. This robust performance underscores its potential for integration into practical substation monitoring systems, where rapid and accurate fault detection is critical for ensuring operational reliability and safety.

Table 6. Classification Accuracy Across Each Fault Type

Fault Type	Problematic Asset	Distance	Accuracy
Loose Connection	Surge Arrester	15m	98.8%
DBA	LBS	15m	100%
	Cap-Pin Ceramic Insulator	25m	75.4%

The performance of the model was further evaluated using precision, recall, and F1 score metrics, providing a comprehensive assessment of its effectiveness in classifying various defect types. For corona detection, the model demonstrated a precision of 80.1%, indicating that 80.1% of its corona predictions were accurate. Additionally, the recall for

corona was remarkably high at 98.8%, demonstrating the model's ability to identify the vast majority of corona occurrences. This resulted in an F1 score of 88.47%, which balances precision and recall by accounting for both false positives and false negatives.

For DBA detection, a precision of 100% was obtained, indicating that all DBA predictions were accurate. The recall for DBA was 87.7%, reflecting the model's capability to detect the vast majority of DBA instances. These metrics combined to yield an F1 score of 93.45%, highlighting the model's performance in classifying DBA defects.

A summary of these results is provided in Table 7. The findings demonstrate the model's reliability in identifying critical defects, particularly DBA, where both precision and F1 score were high.

Table 7. Performance Metric for Each Class Type

Class Type	Recall	Precision	F1 Accuracy
Corona	98.8%	80.1%	88.47%
DBA	87.7%	100%	93.45%

4.2.2.2 Model Interpretability and Analysis

Grad-CAM visualizations provide valuable insights into the classification model's decision-making process by identifying regions of the ultrasonic signal that significantly influence its predictions. As shown in Figure 4.11, the heat map reveals that the model distinctly focuses on the initial high-frequency oscillations in the DBA ultrasonic signal captured from the LBS (15m away) before the signal undergoes damping. This indicates that the model relies heavily on these features for accurate classification.

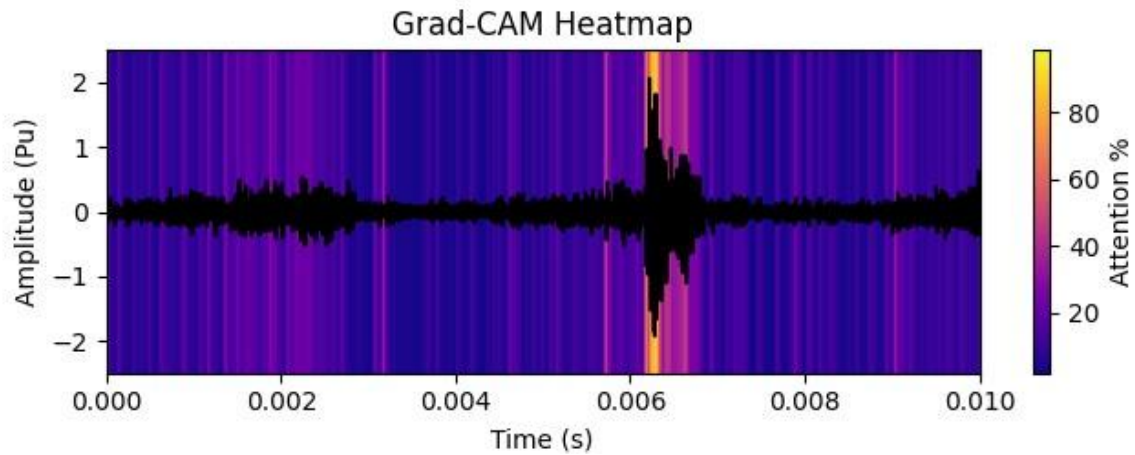


Figure 4.11 Grad-CAM heatmap of DBA signal on the LBS (15m away)

In contrast, misclassified signals, such as those from the cap-pin insulator, illustrate the challenges in identifying critical features over larger distances. For instance, Figure 4.12 demonstrates the application of Grad-CAM to a misclassified sample featuring an attenuated DBA signal from the cap-pin insulator (located 25m away). This visualization shows that the model struggled to focus on specific segments of the signal, highlighting its difficulty in handling attenuated features. These results emphasize the model's sensitivity to signal attenuation and the importance of maintaining signal clarity for accurate classification.

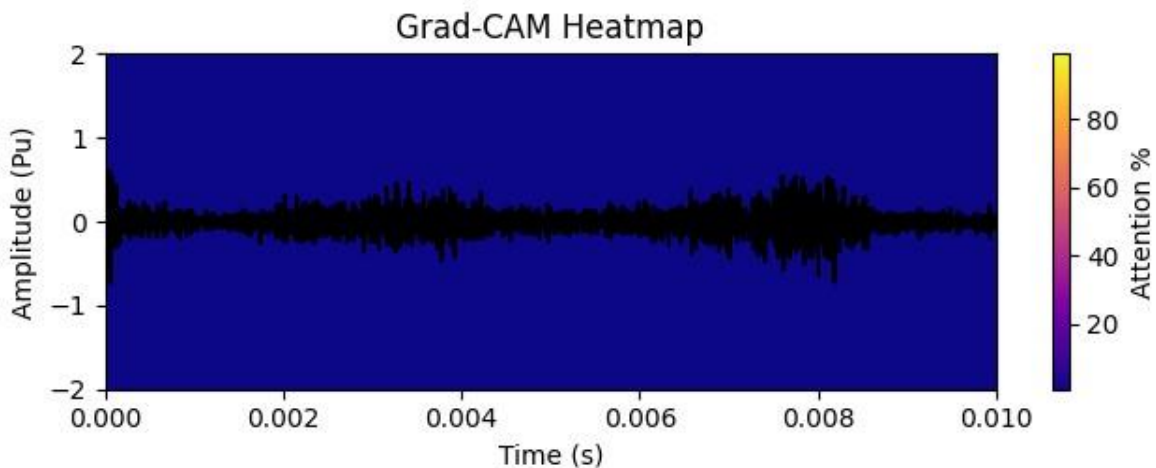


Figure 4.12 Grad-CAM heatmap of a misclassified DBA signal on the cap-pin insulator (25m away)

To further analyze the effects of signal attenuation, a Fast Fourier Transform (FFT) was performed on DBA signals from both the LBS and the cap-pin insulator. The FFT results, presented in Figure 4.13, reveal significant attenuation of signal components across frequencies. Within the audible range (0.02–20 kHz), an approximate reduction of 73.3% was observed, while the ultrasonic range (>20 kHz) exhibited an even higher attenuation of 79.4%. Notably, the most substantial feature loss occurred around 120 kHz, where multiple peaks exceeding 30 pu were completely diminished over longer distances.

This frequency-dependent attenuation is a fundamental characteristic of acoustic wave propagation. Higher-frequency components are more susceptible to energy loss during propagation compared to lower-frequency components. Such attenuation of critical high-frequency features significantly impacts the model's ability to classify signals accurately, particularly over larger distances.

In summary, this analysis underscores the intricate relationship between signal properties, propagation dynamics, and model interpretability. By integrating Grad-CAM visualizations with FFT analysis, it becomes evident that the attenuation of high-frequency features results in substantial feature loss, which directly affects the classification accuracy. These findings highlight the critical need for signal enhancement techniques to mitigate attenuation effects and enhance model performance in real-world scenarios.

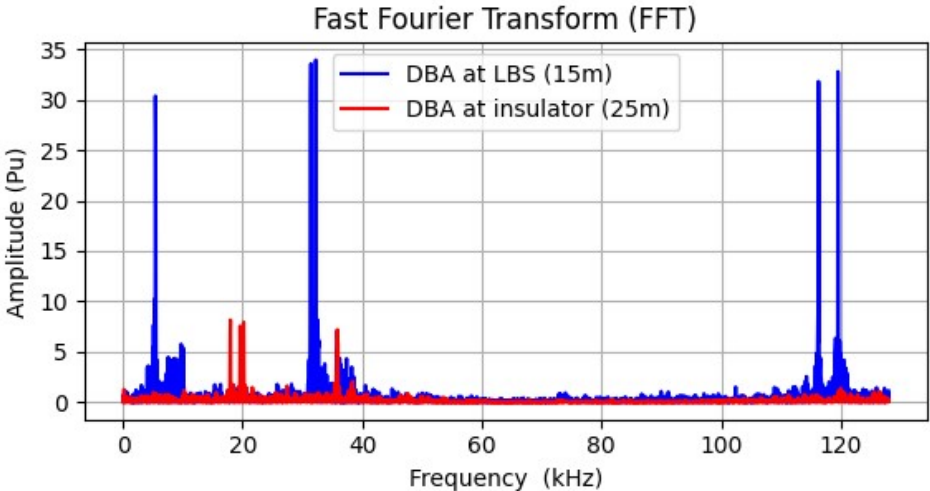


Figure 4.13 FFT of the accurately classified vs misclassified DBA signal at the LBS and cap-pin insulator.

4.3 Multi-Label Classification Results

4.3.1 Performance Evaluation of the Classification Model

The classification model demonstrates excellent performance across all testing datasets, with achieved Hamming scores exceeding 90% in every case. These results underscore the model's robustness and reliability under various conditions.

For combined datasets 1 and 2, evaluated using a 20% test split, the model achieves a Hamming score of 98.4%, as shown in Figure 4.14. This high level of accuracy reflects the similarity in data characteristics between the training and testing subsets, enabling the model to make precise predictions. The consistent conditions across these datasets have significantly contributed to this exceptional performance.

In the case of dataset 3, which involves the two-disc configuration, the model attains a Hamming score of 92%, as depicted in Figure 4.15. Although this score remains excellent, a slight performance reduction is observed due to differences between the test and training conditions. Specifically, the model exhibits some difficulty identifying corona defects, particularly when these appear in combination with DBA. Despite these challenges, the classification capabilities for most defective classes remain robust.

For dataset 4, involving the three-disc configuration, the model achieves a commendable Hamming score of 93.2%, as illustrated in Figure 4.16. While the overall performance is excellent, certain misclassification patterns are observed when corona and internal defects coexist. Specifically, the model often predicts only corona, overlooking the internal defect, and occasionally predicts a combination of corona and internal defects when only corona is present. Nevertheless, these observations highlight opportunities for further refinement to enhance the model's ability to differentiate between defect types with overlapping features.

In summary, the classification model consistently achieves excellent results across all datasets. While minor misclassification patterns are observed, particularly in the corona defect class, the overall performance demonstrates the model's capability to handle diverse scenarios effectively. Future efforts will focus on optimizing the model to further improve its generalization and accuracy.

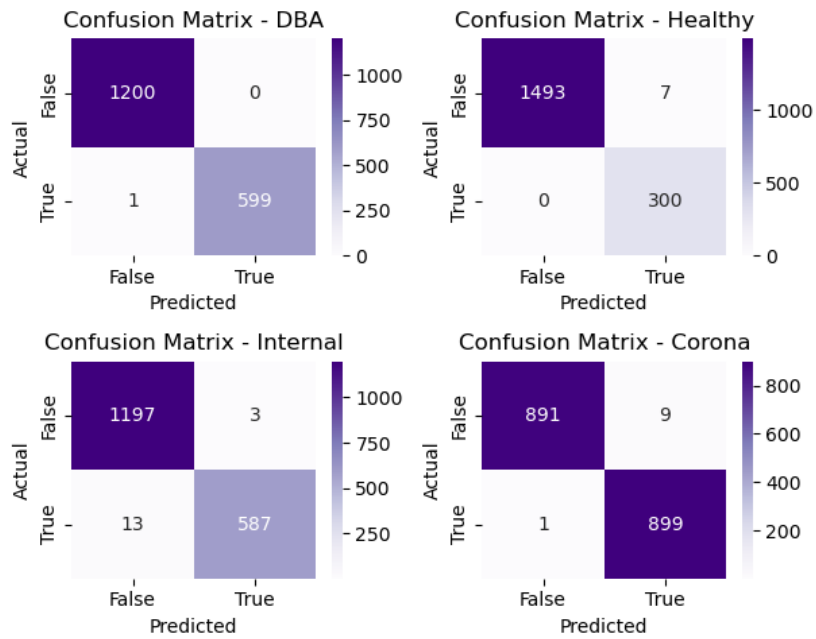


Figure 4.14 Confusion matrices for the 20% test split of combined dataset 1 and 2 (Overall Hamming score 98.4%)

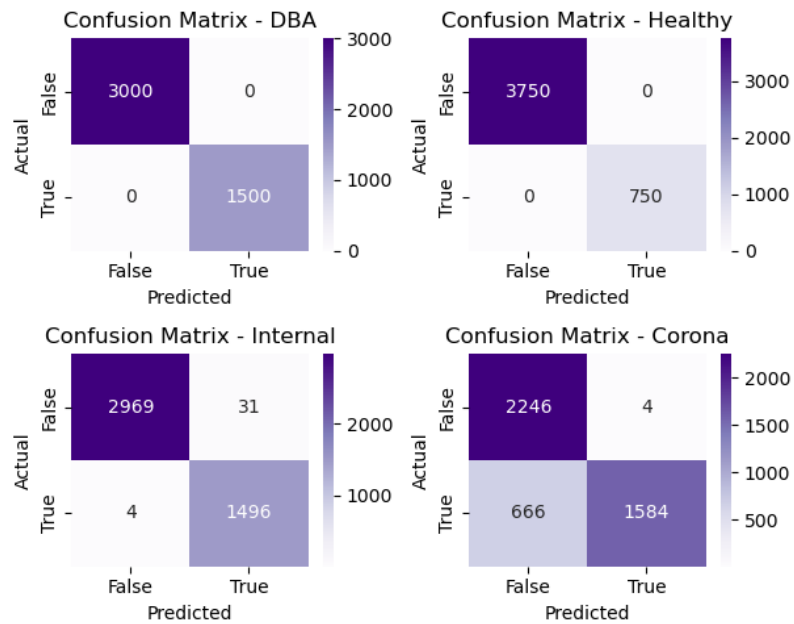


Figure 4.15 Confusion matrices on dataset 3 (Overall Hamming score 92%)

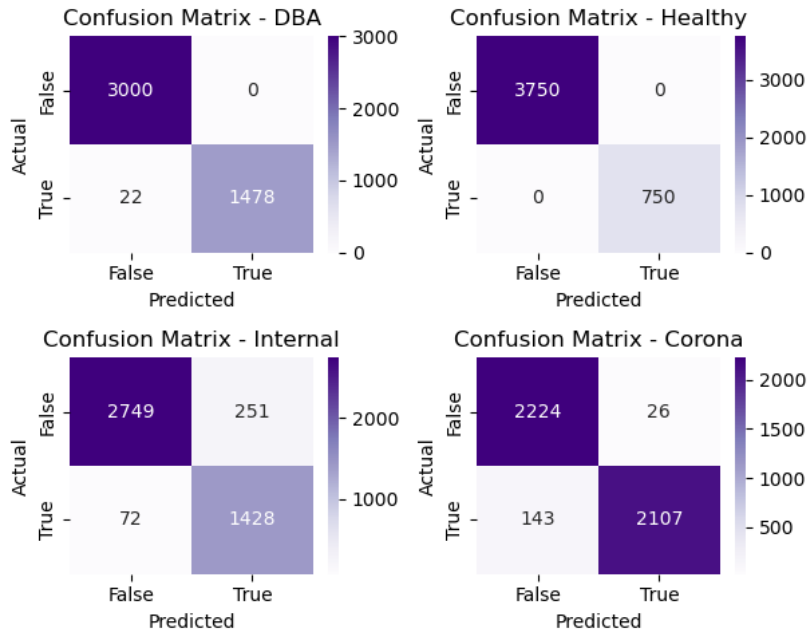


Figure 4.16 Confusion matrices on dataset 4 (Overall Hamming score 93.2%)

4.3.2 Interpretability of CNN Models: Temporal Feature Analysis

To gain a deeper insight into the classification behavior of the proposed CNN model, Grad-CAM was employed to visualize the model’s decision-making framework and interpret the confusion observed between certain classes. Grad-CAM generates heat maps that highlight regions within the ultrasonic signals prioritized by the model during classification. As illustrated in Figures 4.17– 4.20, the CNN consistently focuses on the initial high-frequency oscillations of the discharge, reflecting its increased sensitivity to abrupt amplitude variations. These transient features are critical for defect identification.

For defect-related classes, the model’s attention is predominantly concentrated on these features, whereas for the healthy class, the Grad-CAM results reveal an absence of prominent focal points. This lack of focus can be attributed to the noise-dominated nature of the healthy signals, which lack distinct characteristics necessary for effective classification.

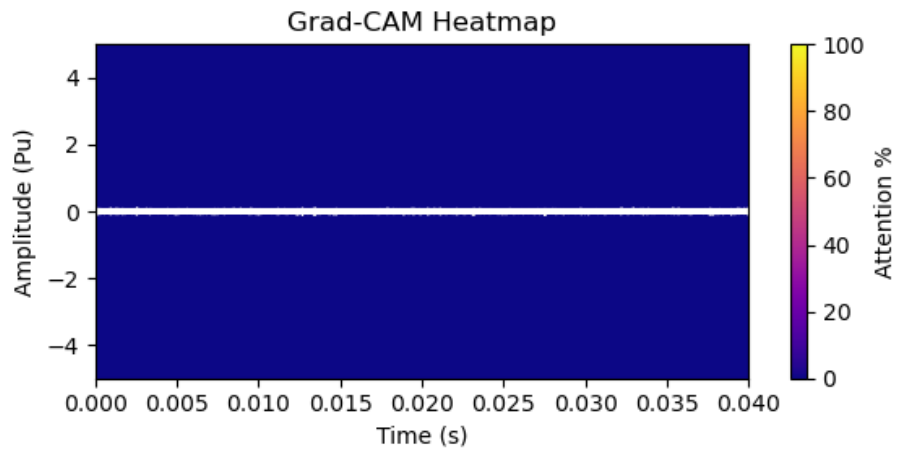


Figure 4.17 Grad-CAM heatmap of healthy insulator signal

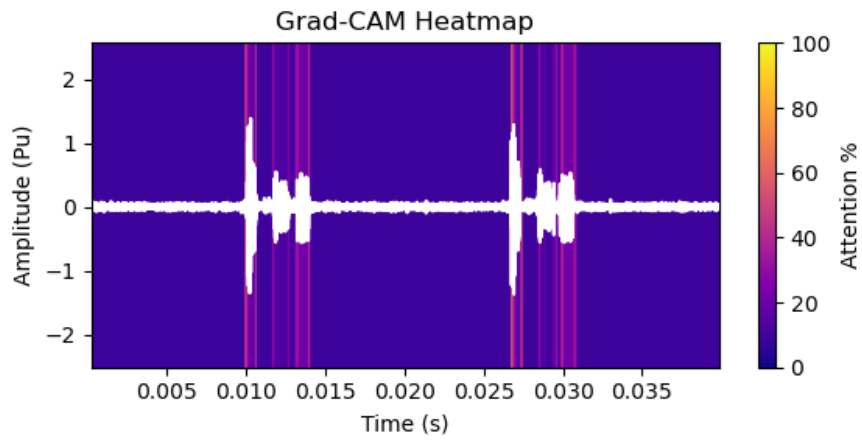


Figure 4.18 Grad-CAM heatmap of Corona signal

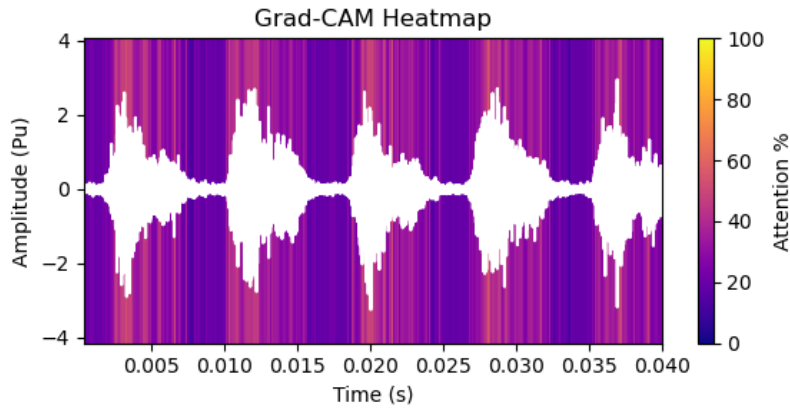


Figure 4.19 Grad-CAM heatmap of DBA signal

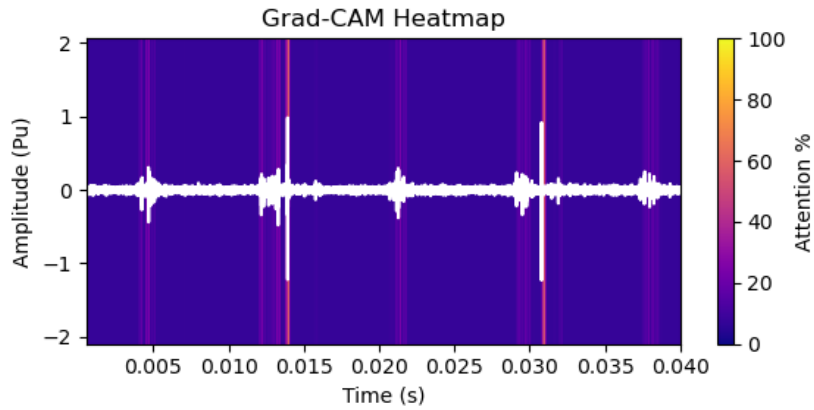


Figure 4.20 Grad-CAM heatmap of Punctured Insulator signal

To build upon these observations, a quantitative analysis was conducted to further characterize the transient features and their role in distinguishing between defect classes. Shannon entropy, a metric that quantifies the randomness or unpredictability within a signal, was employed to evaluate the abrupt changes in signal characteristics. Defective insulators often generate discharges that produce rapid amplitude oscillations, resulting in elevated entropy values. The entropy of a signal is calculated as described in equation (15):

$$H = -\sum_{i=1}^N p_i \log_2(p_i) \quad (15)$$

Where:

- H: Shannon entropy
- N: Total number of unique intensity levels in the signal.
- p_i : Probability of occurrence of the i-th intensity level.

The probabilities p_i are computed as:

$$p_i = \frac{n_i}{\sum_{j=1}^{\omega} n_j} \quad (16)$$

Where:

- n_i : count of occurrences of the i-th intensity level in the signal.
- $\sum_{j=1}^{\omega} n_j$: Total number of samples in the signal.

Furthermore, Grad-CAM analysis revealed that the model primarily concentrated on the transient segments of these discharges. This indicates that each defect class, particularly those classified with high accuracy, exhibits distinct entropy characteristics. A Kernel Density Estimation (KDE) plot of entropy values, derived from 3,750 ultrasonic signals (Figure 4.21), illustrates well-separated distributions corresponding to individual and combined defect classes.

However, the entropy profiles of the corona and internal defect classes exhibit a notable similarity, which can be attributed to the interaction between punctured insulators and neighboring healthy insulators. These interactions give rise to surface discharge activities, a form of PD that closely aligns with the characteristics of corona discharge [60]. Furthermore, the DBA and (DBA + Corona) classes display overlapping entropy patterns, reflecting their shared defect type, DBA. This overlap may explain the model's challenges in distinguishing isolated corona discharge events from those that occur alongside internal defects or DBA.

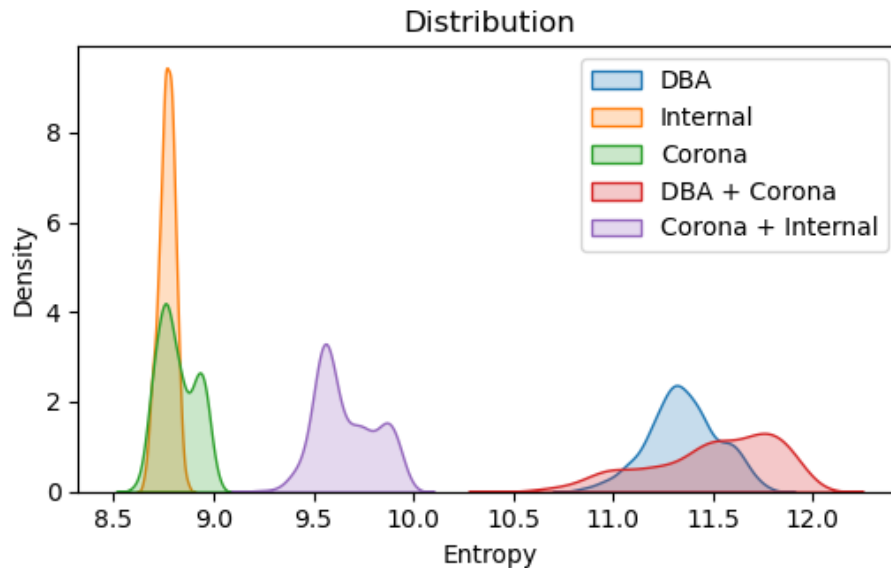


Figure 4.21 KDE plot representing the distribution of Shannon entropy across 3,650 ultrasonic signals of all defect types

Additionally, the regions of attention highlighted by Grad-CAM indicate that the model does not account for the steady-state noise occurring between consecutive discharges. This observation highlights the importance of incorporating additional temporal features, such as discharge duration and repetition intervals, to better understand how the model differentiates between various single and multiple defect types. By capturing and analyzing these timing patterns across all four datasets, this investigation aimed to identify unique temporal characteristics associated with each defect, providing deeper insights into how different defect signatures manifest in both entropy and temporal domains.

The results reveal consistent patterns that further differentiate defect characteristics. For example, corona discharges exhibit a repetition interval of 16 ms, while both DBA and internal discharges occur at intervals of 8 ms. In terms of discharge duration, corona, DBA, and internal discharges persist for 1 ms, 5 ms, and 2 ms, respectively. These temporal attributes remain distinguishable even when multiple defects coexist. For example, when DBA and corona discharges occur simultaneously, their signals can be differentiated based on contrasting repetition intervals, with DBA's rate being twice that of corona.

This relationship allows for the reliable detection of both defects, as two consecutive DBA discharges are typically followed by a corona discharge.

Figure 4.22 illustrates this phenomenon, presenting a sample ultrasonic signal that captures the simultaneous occurrence of DBA and corona discharges on an insulator. This nuanced understanding of temporal features, combined with entropy-based insights, provides a comprehensive framework for defect classification, emphasizing the interplay between transient and temporal domains in identifying complex defect scenarios

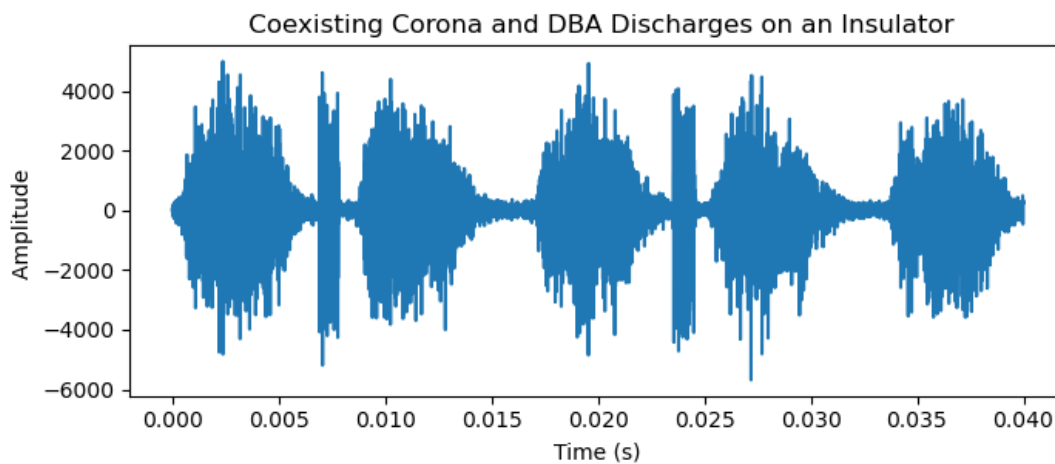


Figure 4.22 Ultrasonic signal showing both DBA and corona on an insulator string

Finally, the energy levels associated with each defect class were computed and analyzed, revealing distinct profiles that align with the underlying physical mechanisms. Among the defects, DBA exhibited the highest energy levels, ranging from 0.2 to 1 p.u². These elevated and highly variable energy ranges reflect the stochastic nature of DBA, which is strongly influenced by surface conditions and wetting profiles. In contrast, corona and internal discharges demonstrated more consistent and comparatively lower energy ranges. Specifically, internal discharge energy levels were observed between 0.005 and 0.025 p.u², while corona energy values ranged from 0.01 to 0.04 p.u².

This closer similarity in the energy profiles of corona and internal discharges provides a plausible explanation for the slight confusion in the classification model, as distinguishing between these two defect types proved to be more challenging. Nevertheless, the systematic characterization of energy levels enhances the interpretability of the model and provides valuable insights into the temporal dynamics of defect activity. Table 8 presents a comprehensive summary of these temporal features, including their respective ranges and associated uncertainties, serving as a foundational reference for further analysis and discussion.

Table 8. Summary of Temporal Features for all Defects

Temporal Features	Corona	DBA	Internal
Shannon Entropy	8.8 ± 0.3	11.3 ± 0.5	8.7 ± 0.1
Energy	$0.025 \pm 0.015 \text{ p.u}^2$	$0.6 \pm 0.4 \text{ p.u}^2$	$0.015 \pm 0.01 \text{ p.u}^2$
Repetition interval or Repetition frequency as a function of power frequency (60Hz)	$16.5 \pm 0.5 \text{ ms}$ 1.01 ± 0.03	$8 \pm 0.5 \text{ ms}$ 2.08 ± 0.13	$8 \pm 0.5 \text{ ms}$ 2.08 ± 0.13
Discharge Length	$1 \pm 0.2 \text{ ms}$	$5 \pm 0.2 \text{ ms}$	$2 \pm 0.2 \text{ ms}$

Chapter 5

Conclusions

5.1 Summary and Conclusions

This thesis demonstrates the substantial potential of ultrasonic sensors, combined with multi-label classification techniques, for diagnosing defects in outdoor ceramic insulators. Although ultrasonic sensors excel at detecting corona and surface discharges, their ability to detect internal discharges is constrained by attenuation effects from porcelain body and metallic caps. To address this challenge, this research introduces an innovative method that utilizes the directional properties of ultrasonic sensors to indirectly detect internally punctured insulators by monitoring surface discharges on adjacent discs. These findings highlight the promise of ultrasonic sensing in outdoor insulator diagnostics, especially when integrated with advanced deep learning models capable of distinguishing between discharge types such as corona, dry band arcing, and surface discharges.

The use of a multi-label classification framework further strengthens diagnostic capabilities by facilitating the accurate identification of both single and co-occurring defects commonly observed in practical scenarios. The model's high classification accuracy stems primarily from its focus on diagnostically significant features, such as the initial high-frequency oscillations of discharge signals, as revealed through Grad-CAM analysis. This emphasis is corroborated by Shannon entropy analysis, which shows that each defect type has a distinct entropy signature, aiding effective classification. Additionally, unique repetition rates and discharge patterns minimize feature overlap in ultrasonic signals, enhancing overall reliability. However, the similarity in entropy and energy profiles between internal and corona discharge can sometimes lead to misclassification of these two defect types.

While these findings underscore the potential for real-time, non-intrusive insulator diagnostics, the study also points to practical considerations for field use. Factors such as signal amplitude and classification accuracy may deteriorate over greater distances, signaling the need for optimized sensor placement strategies and sophisticated data

processing techniques. Despite these limitations, the results offer a strong foundation for advanced diagnostic methods that improve electrical grid reliability, asset management, and operational safety. By combining ultrasonic sensing with deep learning, this work outlines a path toward more accurate and reliable monitoring of high-voltage insulators in complex operational environments.

5.2 Future Work

The future work of this thesis can be broadly categorized into two main areas: enhancing the current approach and exploring new directions. The following subsections will provide a detailed discussion of each.

5.2.1 Enhancing the Current Approach

One limitation of the proposed non-intrusive model is its reduced sensitivity in detecting punctured insulators, particularly in larger insulator strings. For instance, a single punctured disc in a string of 14 insulators may not generate sufficient stress to induce surface discharges for effective detection. Detecting punctured insulators remotely often requires a certain ratio of damaged discs within the string to initiate noticeable surface discharges. Improving the model's sensitivity to detect punctured insulators, even in such scenarios, remains a key area for further development.

Additionally, the multi-label classification model should be validated in real-world field environments. A significant challenge encountered during this research was the absence of field sites with confirmed multiple defects for comprehensive testing. Collaborating with utilities to access defected insulators or conducting controlled field experiments would provide valuable insights into the model's robustness and performance under practical conditions.

Further improvements can also be made in model accuracy and generalization. Incorporating additional data augmentation techniques, experimenting with more advanced deep learning architectures, and employing techniques like transfer learning can enhance the model's adaptability to diverse scenarios.

Evaluating interpretability tools like Grad-CAM in more complex field settings could also strengthen confidence in model predictions.

5.2.2 Exploring New Directions

A promising direction for future research involves a detailed investigation of the frequency content in acoustic signals associated with various insulator defects. Identifying the most influential frequency components could further enhance classification accuracy and offer deeper insights into the underlying physical mechanisms of these defects. A significant challenge, however, is that the acoustic signals generated by insulator defects are inherently non-stationary, making traditional frequency analysis approaches like the Fast Fourier Transform (FFT) less effective due to their assumption of signal stationarity. To address this, advanced time-frequency methods—such as Short-Time Fourier Transform (STFT), Wavelet Transform (WT), or Empirical Mode Decomposition (EMD)—could be employed to better capture the time-varying frequency behavior of non-stationary signals. These techniques would offer a more comprehensive understanding of how specific frequency components correlate with different defect types or stages of progression. Further research might also focus on developing algorithms to automate the extraction and classification of these frequency features, potentially enhancing machine learning model performance in defect detection.

Building on this, another promising direction for future research is to extend the current work to include additional insulator types, particularly polymeric insulators. Unlike their ceramic counterparts, polymeric insulators experience distinct aging mechanisms and degradation modes — such as tracking, erosion, brittle fracture, flash under, chalking, crazing, and cracking [61] — each posing unique diagnostic challenges. Effectively addressing these diverse defects may necessitate refining diagnostic strategies to account for polymeric-specific issues. A particularly effective approach could involve integrating multiple sensing modalities, including acoustic, visual, and electrical, to capture a broader range of defect signatures.

Multi-modal deep learning models offer significant potential in this regard, as they can leverage complex relationships among data from various sensors to enhance diagnostic accuracy and resilience. An example of this application is the FLIR Si2-PD acoustic imaging camera [62], which not only detects acoustic signals from defects but also localizes, classifies, and assesses partial discharge (PD) faults from distances of up to 200 meters. This exemplifies how multi-modal models are already being deployed for advanced defect classification.

Additionally, further research could explore the development of novel sensor technologies or the enhancement of existing ones to better capture the distinct failure modes associated with polymeric insulators. When integrated into multi-modal frameworks, these advancements have the potential to significantly improve diagnostic capabilities in power transmission systems, leading to more reliable and efficient maintenance practices.

References

- [1] S. Sanyal *et al.*, "Replacement Strategy of Insulators Established by Probability of Failure," *Energies*, vol. 13, no. 8, p. 2043, Apr. 2020.
- [2] E. A. Cherney *et al.*, "Evaluation of and Replacement Strategies for Aged High Voltage Porcelain Suspension Type Insulators," in *IEEE Transactions on Power Delivery*, vol. 29, no. 1, pp. 275-282, Feb. 2014.
- [3] Álvarez, F.; Ortego, J.; Garnacho, F.; Sánchez-Urán, M.A. "Advanced techniques for on-line PD measurements in high voltage systems." International Conference on High Voltage Engineering and Application (ICHVE), Poznan, Poland, 8–11 September 2014.
- [4] Álvarez, F.; Garnacho, F.; Albarracín, R.; Granizo, R.; Dong, M.; Ortego, J. "Practical experience of insulation condition evaluation in an on-site HV installation applying a PD measuring procedure." International Conference on Condition Monitoring and Diagnosis (CMD), Xi'an, China, 25–28 September 2016.
- [5] A. Serikbay, M. Bagheri, A. Zollanvari and B. T. Phung, "Accurate Surface Condition Classification of High Voltage Insulators based on Deep Convolutional Neural Networks," in *IEEE Transactions on Dielectrics and Electrical Insulation*, vol. 28, no. 6, pp. 2126-2133, December 2021.
- [6] S. S. Roy, A. Paramane, J. Singh, S. Chatterjee and A. K. Das, "Accurate Sensing of Insulator Surface Contamination Using Customized Convolutional Neural Network," in *IEEE Sensors Letters*, vol. 7, no. 1, pp. 1-4, Jan. 2023.
- [7] D. Sadykova, D. Pernebayeva, M. Bagheri and A. James, "IN-YOLO: Real-Time Detection of Outdoor High Voltage Insulators Using UAV Imaging," in *IEEE Transactions on Power Delivery*, vol. 35, no. 3, pp. 1599-1601, June 2020.
- [8] V. Aksionava, "Pillar with electric wires on a background of Blue Sky," iStock. [Online]. Available: <https://www.istockphoto.com/photo/pillar-with-electric-wires-on-background-of-blue-sky-gm1297375217-390525726>.
- [9] R. S. Gorur, E. A. Cherney, and J. T. Burnham, *Outdoor Insulators*. Phoenix, AZ, USA: Ravi S. Gorur, 1999.
- [10] N. Tonmitr, K. Tonmitr and E. Kaneko, "The Effect of Controlling Stray and Disc Capacitance of Ceramic String Insulator in the Case of Clean and Contaminated Conditions", *Procedia Computer Science*, vol. 86, pp. 333-336, 2016.
- [11] R. E. Macey, W. L. Vosloo, and C. de Turreil, *The Practical Guide to Outdoor High Voltage insulators*. Johannesburg: Crown Publications, 2004.
- [12] Inna, "Modes of failure of line insulators," *INMR*, 20-May-2022. [Online]. Available: <https://www.inmr.com//comparing-failure-modes-of-line-insulators/>

- [13] Lightning and Insulator Subcommittee, "Application of Insulators in a Contaminated Environment," in *IEEE Transactions on Power Apparatus and Systems*, vol. PAS-98, no. 5, pp. 1676-1695, Sept. 1979
- [14] Z. Yuan, Y. Tu, H. Jiang, C. Wang, and C. Wang, "Study on heating mechanism of GRP rod in a composite insulator," *IET Science, Measurement & Technology*, vol. 13, no. 1, pp. 108–113, Jan. 2019.
- [15] U. Shafique *et al.*, "Infrared Thermography-Based Insulator Fault Classification via Unsupervised Clustering and Semi-Supervised Learning," in *IEEE Access*, vol. 12, pp. 180781-180791, 2024.
- [16] F. A. Dewanto, A. M. Khakim, Tumiran, M. Wahyudi, N. A. Setiawan, and D. Saputra, "An approach to assess the 500 kV insulator string condition using ultraviolet imager," *Applied Sciences*, vol. 12, no. 23, p. 12054, 2022.
- [17] S. Wang, M. Zhou and N. Li, "Discharge Ultraviolet Image Characteristics and Insulation State Evaluation of Polluted and Wet Suspension Porcelain Insulator Strings," in *IEEE Transactions on Instrumentation and Measurement*, doi: 10.1109/TIM.2024.3417545.
- [18] C. Shi and Y. Huang, "Cap-Count Guided Weakly Supervised Insulator Cap Missing Detection in Aerial Images," in *IEEE Sensors Journal*, vol. 21, no. 1, pp. 685-691, 1 Jan.1, 2021.
- [19] X. Liu, X. Miao, H. Jiang and J. Chen, "Box-Point Detector: A Diagnosis Method for Insulator Faults in Power Lines Using Aerial Images and Convolutional Neural Networks," in *IEEE Transactions on Power Delivery*, vol. 36, no. 6, pp. 3765-3773, Dec. 2021.
- [20] R. Priatmadja, A. D. Taufiq and M. Nurdin, "Corona Measurement Test in Correlation with Predictive Maintenance on Extra High Voltage Transmission Line," *2020 International Conference on Technology and Policy in Energy and Electric Power (ICT-PEP)*, Bandung, Indonesia, 2020, pp. 236-240
- [21] Frizzo Stefenon, Stefano & Meyer, L.H. "Inspection of Electrical Distribution Network", 2015.
- [22] Inna, "UV & IR imaging of defects in MV/HV components," *INMR*, 26-Nov-2021. [Online]. Available: <https://www.inmr.com/uv-ir-imaging-of-defects-in-hv-components/>.
- [23] A. Darwish *et al.*, "Novel Antenna for Partial Discharge Detection and Classification: A Convolutional Neural Network-Based Deep Learning Approach," in *IEEE Transactions on Dielectrics and Electrical Insulation*, vol. 31, no. 4, pp. 1711-1720, Aug. 2024.
- [24] S. K. Polisetty, A. H. El-Hag, and S. Jayaram, "Partial discharge classification using acoustic signals and artificial neural networks and its application in detection of defects in ceramic insulators," thesis.
- [25] C. F. Kumru, A. Lutfi, A. El-Hag, A. Darwish, S. S. Refaat and H. Abu-Rub, "A Study on the Ability of Different Non-Intrusive Sensors for Diagnosing Outdoor Insulator Defects," *2023 IEEE Electrical Insulation Conference (EIC)*, Quebec City, QC, Canada, 2023, pp. 1-4.

- [26] M. A. S. Masoum, M. A. Imran, and M. R. A. Siddiqui, "Aerial Insulator Inspection using Infrared Thermography," *IEEE Transactions on Dielectrics and Electrical Insulation*, vol. 11, no. 6, pp. 1453-1460, Dec. 2004.
- [27] V. N. Nguyen, R. Jenssen, and D. Roverso, "Intelligent monitoring and inspection of power line components powered by UAVs and deep learning," *IEEE Power Energy Technol. Syst. J.*, vol. 6, no. 1, pp. 11-21, Mar. 2019.
- [28] N. Morozovsky and T. Bewley, "SkySweeper: A low DOF, dynamic high wire robot," in *Proc. IEEE/RSJ Int. Conf. Intell. Robots Syst.*, Nov. 2013, pp. 2339-2344.
- [29] S. Anjum, A. El-Hag, S. Jayaram and A. Naderian, "Classification of defects in ceramic insulators using partial discharge signatures extracted from radio frequency (RF) signals," *2014 IEEE Conference on Electrical Insulation and Dielectric Phenomena (CEIDP)*, 2014, pp. 212-215.
- [30] Miao, X., Liu, X., Chen, J., Zhuang, S., Fan, J. and Jiang, H. "Insulator Detection in Aerial Images for Transmission Line Inspection Using Single Shot Multibox Detector. *IEEE Access* 2019, 7, 9945–9956.
- [31] X. Tao, D. Zhang, Z. Wang, X. Liu, H. Zhang and D. Xu, "Detection of Power Line Insulator Defects Using Aerial Images Analyzed With Convolutional Neural Networks", *IEEE Transactions on Systems, Man, and Cybernetics: Systems*, vol. 50, no. 4, pp. 1486-1498, 2020.
- [32] D. Sarkar and S. Gunturi, "Online health status monitoring of high voltage insulators using deep learning model", *The Visual Computer*, 2021.
- [33] D. Waleed, S. Mukhopadhyay, U. Tariq and A. H. El-Hag, "Drone-Based Ceramic Insulators Condition Monitoring," in *IEEE Transactions on Instrumentation and Measurement*, vol. 70, pp. 1-12, 2021.
- [34] S. Panigrahy and S. Karmakar, "Real-Time Condition Monitoring of Transmission Line Insulators Using the YOLO Object Detection Model With a UAV," in *IEEE Transactions on Instrumentation and Measurement*, vol. 73, pp. 1-9, 2024.
- [35] Z. Zhang, X. Qiao, S. Yang, and X. Jiang, "Non-Uniform Distribution of Contamination on Composite Insulators in HVDC Transmission Lines," *Applied Sciences*, vol. 8, no. 10, p. 1962, Oct. 2018, doi: 10.3390/app8101962.
- [36] "R. Suzuki, WL Vosloo October, 2001 - clumb.free.fr." [Online]. Available: <http://clumb.free.fr/WG11/docs/public/Milan102.pdf>.
- [37] I. Patel *et al.*, "Image Processing Based Estimation of Ceramic Insulator Pollution Levels," *2018 5th International Conference on Electric Power and Energy Conversion Systems (EPECS)*, 2018, pp. 1-4.
- [38] Z. Zhang, H. Zhang, C. Zhou, X. Ma, Y. Li and R. Liu, "A Probabilistic Neural Network Assessment Method for Insulator Pollution Levels Based on Infrared Images," in *IEEE Transactions on Dielectrics and Electrical Insulation*, vol. 31, no. 5, pp. 2711-2720, Oct. 2024.

- [39] Y. Liu, T. Lai, J. Liu, Y. Li, S. Pei and J. Yang, "Insulator Contamination Diagnosis Method Based on Deep Learning Convolutional Neural Network", *2021 3rd Asia Energy and Electrical Engineering Symposium (AEEES)*, 2021. Available: 10.1109/aeees51875.2021.9402970.
- [40] L. Jin and D. Zhang, "Contamination grades recognition of ceramic insulators using fused features of infrared and ultraviolet images," *Energies*, vol. 8, no. 2, pp. 837–858, 2015.
- [41] L. Jin, Z. Tian, J. Ai, Y. Zhang and K. Gao, "Condition Evaluation of the Contaminated Insulators by Visible Light Images Assisted With Infrared Information, in " *IEEE Transactions on Instrumentation and Measurement*, vol. 67, no. 6, pp. 1349-1358, June 2018.
- [42] S. Anjum, S. Jayaram, A. El-Hag and A. Naderian, "Radio frequency (RF) technique for field inspection of porcelain insulators," *2015 IEEE 11th International Conference on the Properties and Applications of Dielectric Materials (ICPADM)*, Sydney, NSW, Australia, 2015, pp. 1019-1022.
- [43] E. Azordegan and B. Kordi, "Remote assessment of high voltage insulators using wideband electromagnetic radiation signature," in *IEEE Transactions on Dielectrics and Electrical Insulation*, vol. 23, no. 3, pp. 1467-1474, June 2016.
- [44] A. E. Lutfi, A. El-Hag and K. Shaban, "Classification of Common Discharges in Outdoor Insulators Using Ultrasonic Signals," *2022 IEEE Conference on Electrical Insulation and Dielectric Phenomena (CEIDP)*, Denver, CO, USA, 2022, pp. 523-526.
- [45] S. Anjum, S. Jayaram, A. El-Hag and A. N. Jahromi, "Detection and classification of defects in ceramic insulators using RF antenna," in *IEEE Transactions on Dielectrics and Electrical Insulation*, vol. 24, no. 1, pp. 183-190, Feb. 2017.
- [46] S. Polisetty, A. El-Hag, and S. Jayram, "Classification of common discharges in outdoor insulation using acoustic signals and Artificial Neural Network," *High Voltage*, vol. 4, no. 4, pp. 333–338, Nov. 2019.
- [47] N. F. Sopelsa Neto et al., "A study of multilayer perceptron networks applied to classification of ceramic insulators using ultrasound," *Applied Sciences*, vol. 11, no. 4, p. 1592, 2021.
- [48] S. Mantach, M. Partyka, V. Pevtsov, A. Ashraf and B. Kordi, "Unsupervised Deep Learning for Detecting Number of Partial Discharge Sources in Stator Bars," in *IEEE Transactions on Dielectrics and Electrical Insulation*, vol. 30, no. 6, pp. 2887-2895, Dec. 2023.
- [49] S. Mantach, A. Ashraf, H. Janani, and B. Kordi, "A convolutional neural network-based model for multi-source and single-source partial discharge pattern classification using only single-source training set," *Energies*, vol. 14, no. 5, p. 1355, 2021.
- [50] Advanced Test Equipment Rentals, "Omicron MPD 600," Accessed: Mar. 23, 2025. [Online]. Available: <https://www.atecorp.com/products/omicron/mpd-600>.
- [51] *IEC 60507*: "Artificial pollution tests on high-voltage ceramic and glass insulators to be used on a.c. systems", 2013.

- [52] M. A. Khan, J. Choo, and Y.-H. Kim, "End-to-end partial discharge detection in power cables via time-domain Convolutional Neural Networks," *Journal of Electrical Engineering & Technology*, vol. 14, no. 3, pp. 1299–1309, 2019.
- [53] S. Mantach, P. Gill, D. R. Oliver, A. Ashraf, and B. Kordi, "An interpretable CNN model for classification of partial discharge waveforms in 3D-printed dielectric samples with different void sizes," *Neural Computing and Applications*, vol. 34, no. 14, pp. 11739–11750, 2022.
- [54] D. P. Kingma and J. Ba, "Adam: A method for stochastic optimization," *arXiv*, Dec. 2014.
- [55] R. R. Selvaraju, M. Cogswell, A. Das, R. Vedantam, D. Parikh and D. Batra, "Grad-CAM: Visual Explanations from Deep Networks via Gradient-Based Localization," *2017 IEEE International Conference on Computer Vision (ICCV)*, Venice, Italy, 2017.
- [56] A. Lutfi, A. El-Hag and K. Shaban, "Non-Intrusive Detection of Ceramic Disc Punctures in Outdoor Insulator Strings," *2024 IEEE Electrical Insulation Conference (EIC)*, Minneapolis, MN, USA, 2024, pp. 217-220.
- [57] C. Yuan, C. Xie, L. Li, F. Zhang and S. M. Gubanski, "Ultrasonic phased array detection of internal defects in composite insulators," in *IEEE Transactions on Dielectrics and Electrical Insulation*, vol. 23, no. 1, pp. 525-531, February 2016
- [58] M. Li, Y. Jing, L. Zhang, X. Li, G. Huang and Z. Wang, "Insulator Defect Detection Based on Ultraviolet Imaging and Acoustic Emission Signal," *2020 IEEE 3rd Student Conference on Electrical Machines and Systems (SCEMS)*, Jinan, China, 2020, pp. 472-475
- [59] H. D. Ilkhechi and M. H. Samimi, "Applications of the Acoustic Method in Partial Discharge Measurement: A Review," in *IEEE Transactions on Dielectrics and Electrical Insulation*, vol. 28, no. 1, pp. 42-51, February 2021.
- [60] D. A. Natrass, "Partial discharge measurement and interpretation," in *IEEE Electrical Insulation Magazine*, vol. 4, no. 3, pp. 10-23, May-June 1988.
- [61] F. Schmuck, I. Gutman, N. Mahatho, M. Perez, A. Phillips, A. Pignini, G. Pirovano, J. Seifert, M. R. Shariati, V. Sklenicka, W. Vosloo, R. Wesley, P. Dulhunty, Z. Kieloch, C. A. M. Nascimento, R. Stephen, and E. Volpov, *Assessment of In-Service Composite Insulators by Using Diagnostic Tools*, Working Group B2.21, CIGRE, Aug. 2013.
- [62] FLIR Systems, "FLIR Si2-PD Industrial Acoustic Imaging Camera," Teledyne FLIR, [Online]. Available: [https://www.flir.ca/products/si2-pd/?vertical=condition+monitoring &segment=solutions](https://www.flir.ca/products/si2-pd/?vertical=condition+monitoring&segment=solutions). [Accessed: Mar. 23, 2025].

Appendix A

List of Papers

Below is a list of publications by the author during doctoral studies.

A1. Journal Papers

- [1] **Abdulla Lutfi**, Ayman El-Hag and Khaled Shaban, "Nonintrusive Ultrasonic Sensing and Deep Learning for Outdoor Ceramic Insulator Assessment," in *IEEE Transactions on Dielectrics and Electrical Insulation*, vol. 31, no. 6, pp. 2993-3000, Dec. 2024, doi: 10.1109/TDEI.2024.3403072.
- [2] Sara Mantach, **Abdulla Lutfi**, Hamed Tavasani, Ahmed Ashraf, Ayman El-Hag, and Behzad Kordi, "Deep Learning in High Voltage Engineering: A Literature Review," *Energies*, vol. 15, no. 14, p. 5005, Jul. 2022. Available: <https://doi.org/10.3390/en15145005>.
- [3] **Abdulla Lutfi**, Ayman El-Hag and Khaled Shaban, "Multi-Label Classification and Acoustic Signature Analysis of Defects in Outdoor Ceramic Insulators," in *IEEE Transactions on Dielectrics and Electrical Insulation*, doi: 10.1109/TDEI.2025.3558194.

A2. Conference Papers

- [4] **Abdulla Lutfi**, Ayman El-Hag and Khaled Shaban, "Classification of Common Discharges in Outdoor Insulators Using Ultrasonic Signals," *2022 IEEE Conference on Electrical Insulation and Dielectric Phenomena (CEIDP)*, Denver, CO, USA, 2022, pp. 523-526, doi: 10.1109/CEIDP55452.2022.9985259.
- [5] **Abdulla Lutfi** and Ayman El-Hag, "Smart Monitoring of Outdoor Insulators," *2022 5th International Conference on Communications, Signal Processing, and their Applications (ICCSPA)*, Cairo, Egypt, 2022, pp. 1-5, doi: 10.1109/ICCSPA55860.2022.10019102.
- [6] Celal Kumru, **Abdulla Lutfi**, Ayman El-Hag, A. Darwish, S. S. Refaat and H. Abu-Rub, "A Study on the Ability of Different Non-Intrusive Sensors for Diagnosing Outdoor Insulator Defects," *2023 IEEE Electrical Insulation Conference (EIC)*, Quebec City, QC, Canada, 2023, pp. 1-4, doi: 10.1109/EIC55835.2023.10177298.
- [7] **Abdulla Lutfi**, Ayman El-Hag and Khaled Shaban, "Non-Intrusive Detection of Ceramic Disc Punctures in Outdoor Insulator Strings," *2024 IEEE Electrical Insulation Conference (EIC)*, Minneapolis, MN, USA, 2024, pp. 217-220, doi: 10.1109/EIC58847.2024.10579282.